Available online at www.agrifarming.org

DOI: http://dx.doi.org/10.18782/2582-7146.309

ISSN: 2582 – 7146

Curr. Rese. Agri. Far. (2026) *7*(2), 8-36

Current Research in Agriculture and Farming

Research Article

Peer-Reviewed, Refereed, Open Access Journal

Green-Engineered Ag/ZnO/Fe_3O_4 Nano-Z-Scheme Derived from Dual Plant Extracts for Visible-Light-Driven Dye Degradation and Multifunctional Biological Applications

Vidusha Singh[1], Indrasheel[2] and Narendra Pratap Singh[1*]

[1]Department of Chemistry, Udai Pratap College, Varanasi-221002, Uttar Pradesh, India

[2]Department of Botany, University of Lucknow, Lucknow-226007, Uttar Pradesh, India

*Corresponding Author E-mail: napratap.singh@gmail.com

Received: 11.02.2026 | Revised: 27.03.2026 | Accepted: 16.04.2026

ABSTRACT

This study reports the green synthesis of a multifunctional Ag/ZnO/Fe3O4 nanocomposite using Murraya koenigii *fruit pods and* Cissus quadrangularis *stem extracts as natural reducing and stabilizing agents. The synthesized nanocomposite was characterized using XRD, FTIR, Raman spectroscopy, UV-Vis spectroscopy, SEM, TEM, DLS, zeta potential, and VSM analyses, confirming its crystalline structure, nanoscale morphology, and soft-ferromagnetic properties. Photocatalytic efficiency under visible light showed significant degradation of Congo Red (87.9%) and Methylene Blue (86.9%) within 120 min, following pseudo-first-order kinetics. Enhanced activity was attributed to efficient charge separation and reactive oxygen species generation through a plasmon-assisted Z-scheme mechanism. The catalyst also exhibited excellent magnetic recoverability and reusability over five cycles. Additionally, notable antibacterial activity against* Pseudomonas aeruginosa *and cytotoxicity toward A549 lung carcinoma cells were observed, demonstrating its potential for sustainable environmental remediation and biomedical applications.*

Keywords: *Green synthesis; Ag/ZnO/Fe_3O_4 nanocomposite; Visible-light photocatalysis; Wastewater treatment; Magnetic recovery; Dye degradation.*

INTRODUCTION

Nanotechnology has emerged as a pivotal platform for the design of advanced multifunctional materials with wide-ranging applications in catalysis, environmental remediation, biomedicine, and pathogen control. In this context, metal and metal-oxide nanocomposites have attracted significant attention owing to their tunable physicochemical properties, large surface-to-volume ratio, and synergistic functionalities arising from the integration of multiple nanoscale components (Agarwal et al. 2017; Alhujaily et al. 2022; Mutukwa et al. 2024).

Cite this article: Singh, V., Indrasheel, & Singh, N.P. (2026). Green-Engineered Ag/ZnO/Fe_3O_4 Nano-Z-Scheme Derived from Dual Plant Extracts for Visible-Light-Driven Dye Degradation and Multifunctional Biological Applications, *Curr. Rese. Agri. Far. 7*(2), 8-36. doi: http://dx.doi.org/10.18782/2582-7146.309

Among these systems, hybrid ternary nanostructures composed of silver (Ag), zinc oxide (ZnO), and iron oxide (Fe_3O_4) demonstrate exceptional performance due to the combined contributions of Ag's plasmonic behaviour, ZnO's semiconducting and photocatalytic nature, and the magnetic recoverability imparted by Fe_3O_4 (Długosz et al. 2021; Wu et al. 2019; Zhang et al. 2021; Shekofteh-Gohari et al. 2015). However, conventional synthesis routes for such nanocomposites often rely on toxic precursors, harsh reducing agents, and energy-intensive conditions, raising serious concerns regarding environmental safety and sustainability.

Green synthesis using plant-derived phytochemicals has therefore emerged as a cleaner, safer, and more sustainable alternative for nanomaterial fabrication (Agarwal et al. 2017; Agarwal et al. 2017). Phytoconstituents such as flavonoids, phenolics, alkaloids, terpenoids, and reducing sugars function as natural reducing, capping, and stabilizing agents, thereby eliminating the need for hazardous chemicals while enhancing biocompatibility (Agarwal et al. 2017; Mutukwa et al. 2024). *Murraya koenigii* (curry leaf) and *Cissus quadrangularis* (Hadjod vine) are medicinal plants well known for their rich phytochemical composition and pronounced antioxidant, anti-inflammatory, and antimicrobial properties. *Murraya koenigii* is particularly rich in carbazole alkaloids, phenolic acids, and flavonoids, whereas *Cissus quadrangularis* contains stilbenes, triterpenoids, and ascorbic acid derivatives, all of which exhibit strong reducing and chelating capabilities (Alam et al. 2014; Nazneen et al. 2020; Kalpana et al. 2017; Nocedo-Mena et al. 2024). The use of a combined (1:1) extract enhances the diversity and density of active phytochemicals, thereby improving nucleation efficiency, particle stability, and structural uniformity during green nanocomposite formation.

Green-synthesized ZnO-based hybrid nanocomposites have been widely explored for visible-light-driven photocatalytic degradation of organic dyes, owing to their enhanced charge separation and surface reactivity (Asadullah et al. 2020). The integration of Ag, ZnO, and Fe_3O_4 into a single nanocomposite further amplifies multi-functionality. Ag nanoparticles are widely recognized for their potent antimicrobial efficacy and localized surface plasmon resonance, ZnO contributes wide band-gap semiconducting behaviour and photocatalytic reactivity under UV-visible irradiation, while Fe_3O_4 provides magnetic properties that facilitate easy recovery and enhance electron transport dynamics (Długosz et al. 2021; Wu et al. 2019; Zhang et al. 2021). The resulting Ag/ZnO/Fe_3O_4 hybrid system exhibits improved charge-carrier separation efficiency, enhanced reactive oxygen species (ROS) generation, and superior surface reactivity; key factors governing catalytic degradation, microbial inhibition, antioxidant activity, and cancer cell apoptosis (Shekofteh-Gohari et al. 2015; Sponza and Korkmaz 2023; Mamba et al. 2024; Goudjil et al. 2024).

1.1 Role of alkaloids in nanocomposite synthesis

Alkaloids are nitrogen-containing heterocyclic phytochemicals that play a crucial role in green nanomaterial synthesis. Their electron-rich nitrogen atoms, aromatic frameworks, and functional groups (–NH, $–N^+$, $–OCH_3$) enable efficient reduction of metal ions, particularly Ag^+ and Fe^{3+}, thereby accelerating nucleation and promoting controlled crystal growth (Elamin et al. 2022). Carbazole alkaloids derived from *Murraya koenigii* exhibit strong affinity toward nanoparticle surfaces, acting as bio-capping and stabilizing agents that prevent agglomeration and enhance dispersion stability in aqueous media (Devadoss et al. 2023). Additionally, alkaloids participate in the chelation of Zn^{2+} and Fe^{3+} ions, facilitating homogeneous incorporation into the

ZnO/Fe_3O_4 lattice and promoting the formation of a stable ternary nanocomposite network. Their intrinsic antioxidant and redox-active nature further supports the generation of smaller, uniformly distributed nanoparticles with improved crystallinity (Bhardwaj et al. 2024).

1.2 Significance of the Ag/ZnO/Fe_3O_4 green-synthesized nanocomposite

The ternary $Ag/ZnO/Fe_3O_4$ nanocomposite synthesized using dual plant extracts uniquely integrates plasmonic, magnetic, and semiconducting functionalities within a single framework. Recent studies have demonstrated that *Murraya koenigii* mediated zinc oxide nanoparticles exhibit strong antibacterial and bioactive properties, highlighting the therapeutic relevance of plant-assisted green synthesis routes (Asadullah et al. 2025). In ternary $Ag/ZnO/Fe_3O_4$ nanocomposite: Ag enhances interfacial charge separation, ZnO contributes photocatalytic and antibacterial activity (Takcı et al. 2024), and Fe_3O_4 introduces magnetism while improving electron mobility across the heterojunction interface (Długosz et al. 2021; Wu et al. 2019; Zhang et al. 2021). Such multifunctional integration results in enhanced ROS generation, improved surface reactivity, and reduced electron-hole recombination rates features critical for environmental and biomedical applications.

Comprehensive physicochemical characterization is essential to validate both the synthesis mechanism and functional attributes of these nanocomposites. FTIR spectroscopy identifies phytochemical functional groups responsible for metal-ion reduction and surface capping (Kanimozhi et al. 2022). X-ray diffraction (XRD) confirms crystalline phases, structural purity, and average crystallite size, while Raman spectroscopy provides vibrational insights into metal–oxide interactions. Vibrating sample magnetometry (VSM) evaluates magnetic behaviour arising from Fe_3O_4 incorporation, whereas surface morphology and elemental distribution are analysed using scanning electron microscopy (SEM), transmission electron microscopy (TEM), and energy-dispersive X-ray spectroscopy (EDX). Furthermore, dynamic light scattering (DLS) and zeta potential analyses offer valuable information on hydrodynamic size distribution and colloidal stability (Długosz et al. 2021).

1.3 Biological and photocatalytic potential

Green-synthesized $Ag/ZnO/Fe_3O_4$ nanocomposites exhibit pronounced biological activity due to synergistic interactions between metallic domains and surface-bound phytochemicals. Their antioxidant potential, evaluated through DPPH radical scavenging assays, arises from electron-donating phyto-metabolites and redox-active metal oxides (Blois 1958; Kedare and Singh 2011; Gulçin 2023). The nanocomposites demonstrate strong antimicrobial efficacy, particularly against *Pseudomonas aeruginosa*, attributed to membrane disruption, enhanced ROS production, and Ag-mediated bio-molecular interactions (Wu et al. 2019; Bauer et al. 1966; Khan et al. 2019). In anticancer studies, the hybrid nanoparticles induce oxidative stress, mitochondrial dysfunction, and apoptosis in A549 lung carcinoma cells, an effect further enhanced by bioactive alkaloids and flavonoids adsorbed on the nanoparticle surface (Zhang et al. 2021; Mosmann 1983).

In addition to biological applications, the nanocomposite exhibits excellent photocatalytic performance under light irradiation, effectively degrading both cationic (methylene blue) and anionic (Congo red) dye pollutants. The synergistic interaction of plasmonic Ag, ZnO semiconductor activity, and Fe_3O_4-mediated electron transfer significantly enhances charge separation and accelerates dye mineralization pathways (Shekofteh-Gohari et al. 2015; Sponza and Korkmaz 2023; Langmuir 1918; Ho and McKay 1999).

Overall, the green synthesis of Ag/ZnO/Fe_3O_4 nanocomposites using a dual-plant extract blend of *Murraya koenigii* and *Cissus quadrangularis* represents an eco-friendly, cost-effective, and highly versatile strategy for engineering multifunctional nanomaterials. Their integrated structural, optical, magnetic, and biological performance positions them as promising candidates for next-generation biomedical interventions and sustainable environmental remediation technologies. This study systematically reports the synthesis, multi-technique characterization, and comprehensive biological and photocatalytic evaluation of these novel green-engineered nanocomposites.

MATERIALS AND METHODS

2.1 Synthesis of extract:

Fruit pods of *Murraya koenigii* and stems of *Cissus quadrangularis* were collected and thoroughly washed with double-distilled (DD) water to remove adhering dust and surface contaminants. The cleaned plant materials were sun-dried for eight days and subsequently ground into a fine powder using a mechanical grinder.

Equal quantities of the powdered fruit pods of *Murraya koenigii* and stems of *Cissus quadrangularis* were mixed in a 1:1 ratio. A total of 10 g of the mixed powder was added to 100 mL of double-distilled water and heated at 60 °C for approximately 45 min until the volume was reduced to half of its initial volume. The extract was then filtered using Whatman No. 42 filter paper to remove particulate matter. The filtrate was stored at 4 °C for 24 h. After refrigeration, the extract was reheated at 60 °C and used for the synthesis of nanocomposites.

2.2 Synthesis of nanocomposite:

A 1:1 mixture of aqueous extract of fruit pods of *Murraya koenigii* and aqueous extract of stem of *Cissus quadrangularis* was heated to 60°C, followed by sequential addition of 0.1 M $AgNO_3$, Zinc acetate, and $FeCl_3$ solutions at 11.5 pH (maintained by adding 0.1M NaOH solution) under constant stirring for 1 h (Fig.1). The solution gradually turned dark brown, indicating nanoparticle formation driven by phytochemical-mediated reduction (Agarwal et al. 2017; Agarwal et al. 2017; Alam et al. 2014; Nazneen et al. 2020; Kalpana et al. 2017; Bhardwaj et al. 2024).

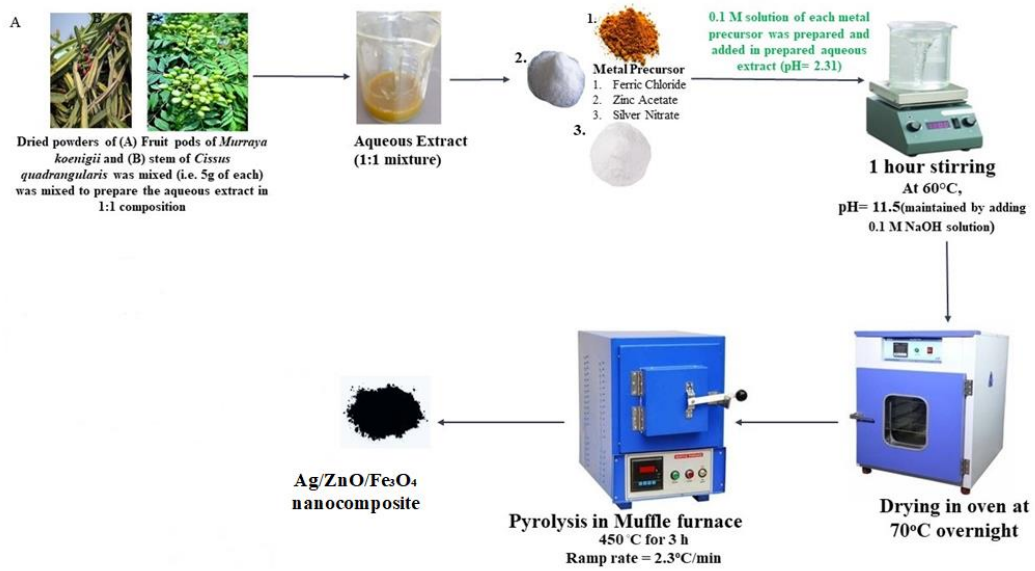

Fig (1): Schematic illustration of the green synthesis route employed for the preparation of the Ag/ZnO/Fe_3O_4 nanocomposite using aqueous extract of fruit pods of *Murraya koenigii* and stems of *Cissus quadrangularis* in 1:1 ratio.

The product was centrifuged, washed repeatedly with deionized water and ethanol to remove unbound biomolecules, and oven-dried overnight at 70°C. The dried material was calcined at 450°C in muffle furnace for 3 h to enhance crystallinity and improve catalytic stability (Długosz et al. 2021; Wu et al. 2019; Zhang et al. 2021; Shekofteh-Gohari et al. 2015).

2.3 Biological Activity:

(a) DPPH free radical scavenging assay

The antioxidant activity of the $Ag/ZnO/Fe_3O_4$ nanocomposite was evaluated using the standard 2,2-diphenyl-1-picrylhydrazyl (DPPH) radical scavenging method (Blois 1958; Kedare and Singh 2011; Gulçin 2023). A series of concentrations (1-1000 µg/mL) of the nanocomposite were mixed with freshly prepared DPPH solution (0.1 mM in methanol) and incubated in the dark for 30 minutes. Absorbance was measured at 517 nm using a UV-Vis spectrophotometer. Ascorbic acid served as the positive control. Percentage scavenging was calculated using:

$$\% \, Inhibition = \frac{A_0 - A_s}{A_0} \times 100 \qquad \ldots\ldots\ldots\ldots (i)$$

where A_0= control and A_s= sample absorbance. IC_{50} values were determined from concentration-inhibition plots.

(b) MTT cytotoxicity assay (A549 Lung carcinoma cells)

The cytotoxic potential of the $Ag/ZnO/Fe_3O_4$ nanocomposite was assessed using the MTT [3-(4,5-dimethylthiazol-2-yl)-2,5-diphenyltetrazolium bromide] assay following the standard protocol described by Mosmann (1983). Human lung carcinoma A549 cells were seeded in 96-well plates at a density of 1×10^4 cells per well and incubated for 24 h to allow cell attachment. The cells were then treated with varying concentrations of the nanocomposite (1-1000 µg/mL) for 24 h. After treatment, 20 µL of MTT (5 mg/mL) was added to each well and incubated for 4 h. Formazan crystals were dissolved using DMSO, and absorbance was measured at 570 nm. Cell viability (%) was calculated relative to the untreated control.

(c) Antibacterial activity (disc diffusion method)

Antibacterial activity against *Pseudomonas aeruginosa* (MTCC 3541) was assessed using the Kirby-Bauer disc diffusion assay (Bauer et al. 1966; Khan et al. 2019). Sterile filter discs were loaded with 62.5 µg/disc of the nanocomposite, air-dried, and placed on Mueller-Hinton agar plates inoculated with the test bacterium. Ciprofloxacin (10 µg/disc) was used as the positive control. Plates were incubated at 37°C for 24 h, and zones of inhibition (mm) were measured.

2.4 Photocatalytic Activity

2.3.1 Preparation of dye solutions

Congo Red (CR, anionic azo dye) and Methylene Blue (MB, cationic thiazine dye) were used as model pollutants. Stock solutions (100 mg/L) were prepared in distilled water and diluted to 20 mg/L for all experiments. The solutions exhibited characteristic absorption maxima at ~497 nm (CR) and ~664 nm (MB) (Shekofteh-Gohari et al. 2015; Zhang et al. 2021; Sponza and Korkmaz 2023).

2.3.2 Photocatalytic reactor setup

The photocatalytic activity of the green-synthesized $Ag/ZnO/Fe_3O_4$ nanocomposite was evaluated using two model organic dyes Congo Red (CR, anionic) and Methylene Blue (MB, cationic) under visible-light irradiation (Długosz et al. 2021; Wu et al. 2019; Zhang et al. 2021). For all experiments, a stock dye solution (50 mg/L) was freshly prepared using deionized water, and required concentrations were obtained by serial dilution. In a typical degradation experiment, 50 mL of dye solution was transferred to a borosilicate reactor, and 25 mg of the nanocomposite was added under continuous magnetic stirring to ensure uniform dispersion. Prior to illumination, the suspension was stirred in the dark for 30 minutes to establish adsorption-desorption equilibrium between dye molecules and catalyst surface.

Visible-light irradiation was provided using a 300 W xenon lamp equipped with a 420 nm cut-off filter, ensuring exclusion of UV wavelengths. During the photocatalytic run, aliquots (2 mL) were collected at predetermined time intervals (0-120 min), centrifuged to remove catalyst particles, and the supernatant was analyzed using UV-Vis spectroscopy (350-800 nm). Dye concentration was estimated based on absorbance at 497 nm for CR and 664 nm for MB, and degradation efficiency was calculated using:

$$\% \, Degradation = 1 - \frac{C_t}{C_0} \times 100 \qquad \ldots\ldots\ldots\ldots (ii)$$

where C_0 and C_t denote initial and time-dependent dye concentrations derived from their respective absorbance values (Langmuir 1918; Ho and McKay 1999).

Kinetic behaviour was modelled using the Langmuir-Hinshelwood pseudo-first-order rate equation by plotting $\ln(C_0/C_t)$ versus irradiation time. Adsorption characteristics prior to photocatalysis were assessed via equilibrium isotherm experiments using varied dye concentrations (10-60 mg/L), and the adsorption capacity (q_e) was calculated to construct Langmuir plots (C_e/q_e vs. C_e) (Langmuir 1918; Ho and McKay 1999). The reusability of the catalyst was evaluated over five successive degradation cycles. After each run, the nanocomposite was collected using a neodymium bar magnet, washed thoroughly with deionized water and ethanol, dried at 60°C for 2 hours, and reused under identical conditions. No additional regeneration agents were employed to ensure realistic assessment of catalyst durability (Długosz et al. 2021; Wu et al. 2019).

All experimental measurements were conducted in triplicate to ensure reproducibility, and the reported values represent averaged results.

3. Characterization and Results & Discussion

3.1.1 UV-Vis absorption behaviour

The optical characteristics of the biosynthesized Ag/ZnO/Fe_3O_4 nanocomposite were examined using UV-Vis absorption spectroscopy (Fig. 2(a)). The smoothed spectrum exhibits a broad and continuous absorption profile across both the UV and visible regions, without a sharp localized surface plasmon resonance (LSPR) peak typically associated with isolated Ag nanoparticles. This spectral pattern confirms strong electronic coupling among Ag, ZnO and Fe_3O_4, indicating the formation of an integrated hybrid nanostructure rather than a physical mixture of independent components (Długosz et al. 2021; Wu et al. 2019).The persistent visible-range absorption tail is attributed to oxygen vacancies, Fe^{3+}-O^{2-} charge-transfer transitions and defect-induced electronic states generated during green synthesis, all of which support the incorporation of synergistic plasmonic-semiconducting-magnetic domains within the ternary composite (Długosz et al. 2021; Wu et al. 2019; Zhang et al. 2021; Shekofteh-Gohari et al. 2015).

3.1.2 Band-gap estimation

The optical band gap (E_g) of the nanocomposite was determined using the Tauc relation for a direct allowed transition, plotted as $(\alpha h\nu)^2$ versus photon energy (Fig. 2(b)) (Długosz et al. 2021; Wu et al. 2019). Linear extrapolation of the high-energy region yielded an optical band gap of approximately 2.07 eV, which is markedly lower than the intrinsic value of 3.20 eV for bulk ZnO. The band-gap narrowing arises from a combination of cooperative factors: (i) Ag-ZnO plasmonic coupling, which enhances charge transfer and improves visible light absorption; (ii) Fe_3O_4-derived mid-gap states originating from Fe^{2+}/Fe^{3+} hopping and spinel-lattice defects; and (iii) oxygen vacancies and phytochemical capping effects, which introduce localized electronic states within the forbidden region (Długosz et al. 2021; Wu et al. 2019; Zhang et al. 2021; Shekofteh-Gohari et al. 2015; Sponza and Korkmaz 2023).Together, these mechanisms modify the electronic band structure of ZnO, leading to strong absorption in the visible region.

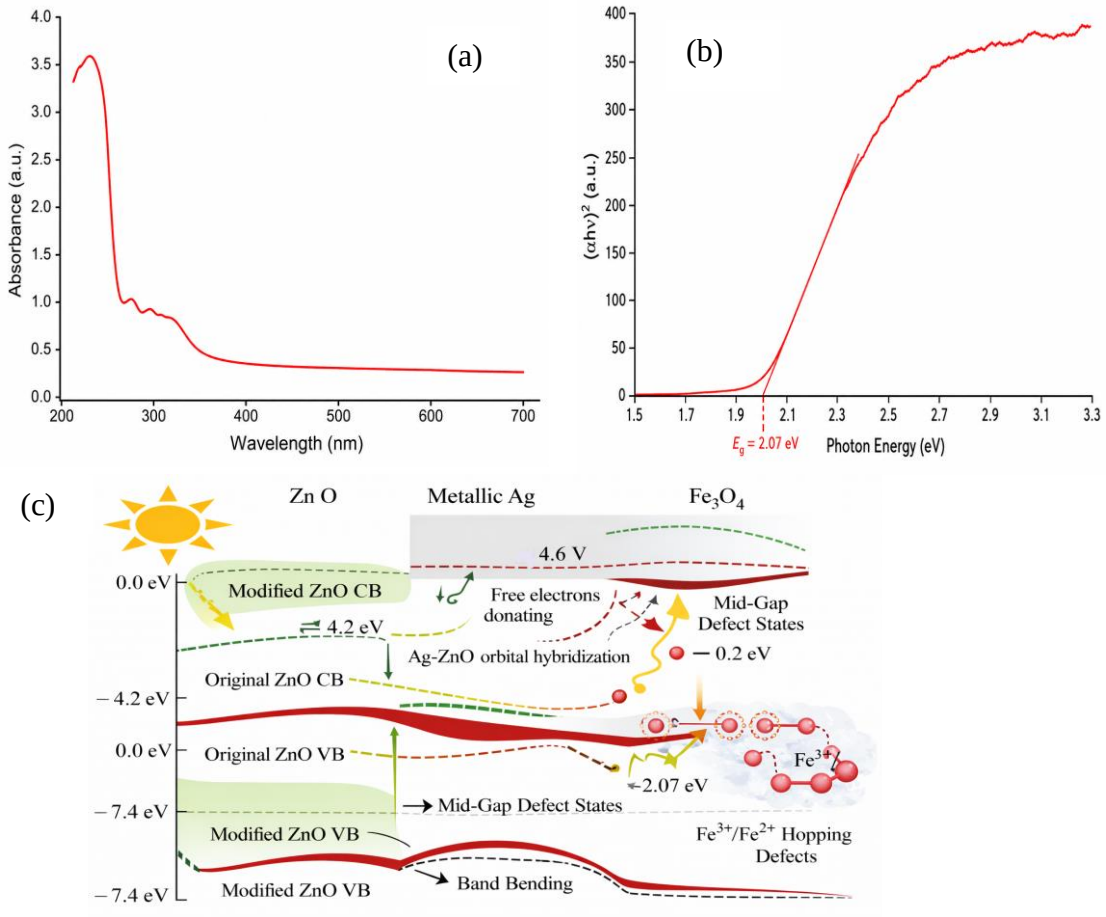

Fig (2): UV-visible absorption spectrum and optical band gap estimation of the synthesized Ag/ZnO/Fe_3O_4 nanocomposite. (a) UV-Vis absorption spectrum recorded in the wavelength range of 200-700 nm. (b) Tauc plot $(\alpha h\nu)^2$ versus photon energy (hv) used to estimate the direct optical band gap of the nanocomposite. (c) Schematic energy band diagram illustrating band-gap narrowing and interfacial charge-transfer mechanisms in the Ag/ZnO/Fe_3O_4 nanocomposite.

3.1.3 Schematic interpretation of band-gap narrowing

Prior to composite formation, ZnO possesses a wide band gap (3.2 eV) with a conduction band (CB) positioned at approximately -4.2 eV and a valence band (VB) at -7.4 eV. Fe_3O_4 exhibits a very narrow gap (~0.1-0.2 eV) and provides Fe^{2+}/Fe^{3+} hopping-associated mid-gap defect levels, whereas metallic Ag functions as an electron sink with a Fermi level positioned between the CB and VB of ZnO [18-22]. Following nanocomposite formation, Ag contributes free electrons to ZnO and raises its Fermi level, while Fe_3O_4 introduces additional internal defect states. Simultaneously, oxygen vacancies generated during green synthesis further compress the band structure. As a result, the conduction band shifts downward slightly due to Ag-ZnO orbital hybridization, the valence band shifts upward due to Fe–O defect complexes, and mid-gap states evolve within the forbidden region ultimately reducing the effective band gap to ~2.07 eV (Długosz et al. 2021; Wu et al. 2019; Zhang et al. 2021; Shekofteh-Gohari et al. 2015) (Fig.2(c)). The corresponding schematic band diagram (Fig. 2(c)) illustrates (i) the modified CB and VB positions of ZnO after hybridization, (ii) Fermi-level alignment of Ag, (iii) Fe_3O_4 induced mid-gap defect states, (iv) band bending at the interfaces, and (v) electron-transfer pathways responsible for visible-light activation (Długosz et al. 2021; Wu et al. 2019; Zhang et al. 2021; Shekofteh-Gohari et al. 2015).

3.2 X-ray diffraction (XRD)

The XRD analysis of the synthesized Ag/ZnO/Fe_3O_4 nanocomposite reveals a well-defined multiphase crystalline structure consisting of Fe_3O_4, ZnO, and metallic Ag, as confirmed by peak positions, d-spacings, and plane indexing (Długosz et al. 2021; Zhang et al. 2021; Shekofteh-Gohari et al. 2015). The strong reflections observed at 2θ = 27.36°, 30.20°, 43.10°, 57.46°, and 62.56° (Fig. 3), corresponding to the (220), (311), (400), (511), and (440) planes, respectively, match well with the standard magnetite phase Fe_3O_4 (JCPDS No. 19-0629). These peaks exhibit d-spacing between 1.48-3.26 Å, with crystallite sizes ranging from 49-92 nm, and microstrain values of 1.40-2.80×10^{-3}, confirming the presence of defect-rich, nanocrystalline spinel ferrite domains. Similarly, the diffraction peaks at 31.77°, 34.42°, and 36.25°, indexed to the (100), (002), and (101) planes of wurtzite ZnO, align closely with the standard hexagonal ZnO pattern (JCPDS No. 36-1451).The calculated d-spacing (2.81-2.47 Å), crystallite size calculated from representative peaks using the Debye-Scherrer equation fell in the range of ~54-92 nm, with an average size of ~65 nm, confirming the nanocrystalline character of the composite, and microstrain values in the range 1.95-2.35×10^{-3} indicate the presence of highly crystalline ZnO nanoparticles without significant lattice distortion (Długosz et al. 2021; Zhang et al. 2021; Shekofteh-Gohari et al. 2015).

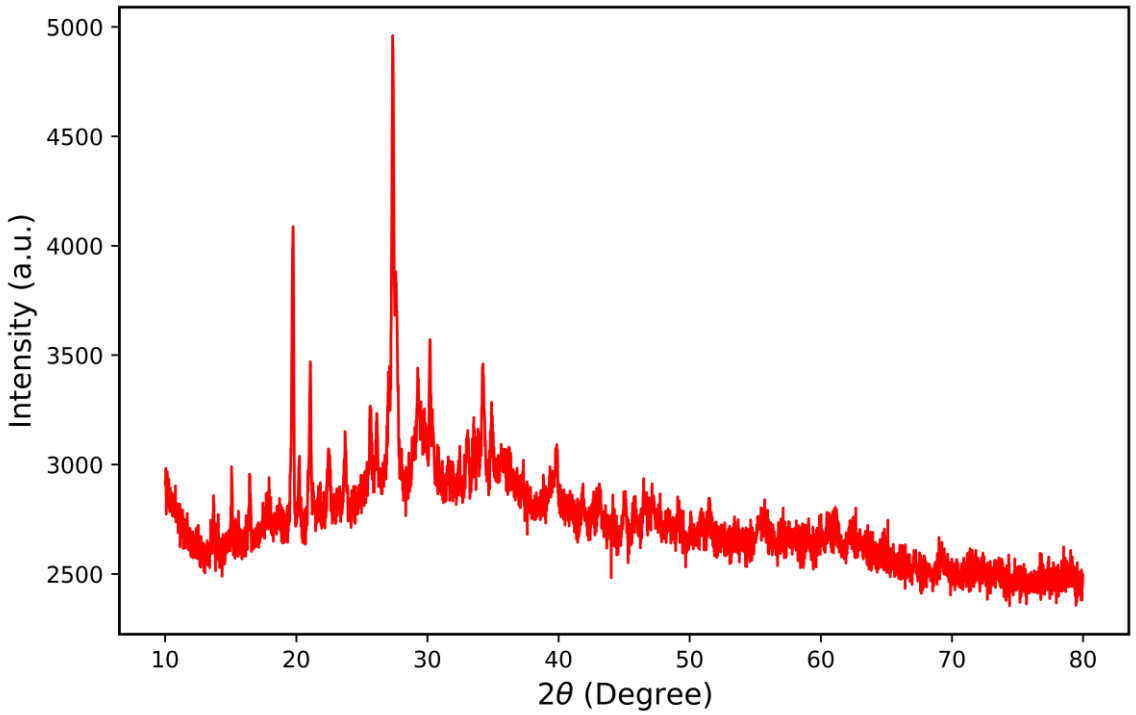

Fig (3): XRD pattern of the synthesized Ag/ZnO/Fe_3O_4 nanocomposite. The diffraction peaks at 2θ ≈ 31.7°, 34.4°, and 36.2° are indexed to the (100), (002), and (101) crystallographic planes of wurtzite ZnO (JCPDS No. 36-1451). The reflections observed at 2θ ≈ 24.1°, 33.2°, and 35.6° correspond to the characteristic planes of Fe_3O_4, while the sharp peak at 2θ ≈ 38.1° is attributed to the (111) plane of face-centered cubic Ag (JCPDS No. 04-0783). The absence of impurity peaks and the presence of all characteristic reflections indicate the successful synthesis and good crystalline nature of the Ag/ZnO/Fe_3O_4 nanocomposite.

A distinct peak at 38.12°, assigned to the (111) plane of metallic silver, corresponds to the face-centered cubic structure of Ag (JCPDS No. 04-0783), confirming the successful incorporation of Ag nanoparticles within the composite. This peak exhibits a crystallite size of ~55 nm, consistent with plasmonically active, nanoscale silver domains (Długosz et al. 2021; Zhang et al. 2021; Shekofteh-Gohari et al. 2015). The calculated dislocation density

values (1.18-4.16×10^{-4} nm^{-2}) across all phases confirm a high density of crystalline imperfections, typical for green-synthesized, multi-component nanocomposites where rapid nucleation and interfacial coupling occur simultaneously. Overall, the combination of indexed reflections, crystallite sizes (49-92 nm), microstrain profiles, and dislocation densities validates the formation of a true ternary Ag/ZnO/Fe_3O_4 nanocomposite, rather than a physical mixture, with each phase maintaining its crystallographic identity as supported by the corresponding JCPDS cards (Długosz et al. 2021; Zhang et al. 2021; Shekofteh-Gohari et al. 2015).

3.2 Fourier transform infrared spectroscopy (FTIR)

The FTIR spectrum of the biosynthesized Ag/ZnO/Fe_3O_4 nanocomposite displays several distinct vibrational bands that collectively confirm successful formation of the ternary hybrid system (Fig: 4). A broad, intense band centered around ~3350 cm^{-1} corresponds to O–H and N–H stretching vibrations originating from polyphenols and alkaloids in the plant extract, indicating their active role as natural reducing and capping agents (Agarwal et al. 2017; Alam et al. 2014; Nazneen et al. 2020; Kalpana et al. 2017). The well-resolved absorption at ~1630 cm^{-1} arises from amide-I (C=O) and H–O–H bending modes, associated with proteinaceous and flavonoid components responsible for biomolecular stabilization of the nanoparticles. Peaks in the ~1380-1400 cm^{-1} region (C–H bending) and those at ~1250-1180 cm^{-1} (C–O–C stretching) reflect the presence of alkyl and ether linkages from polysaccharides, while the absorption around ~1100 cm^{-1} corresponds to C–N/C–O stretching, indicating surface functionalization by aliphatic amines or alcohols (Długosz et al. 2021; Zhang et al. 2021).

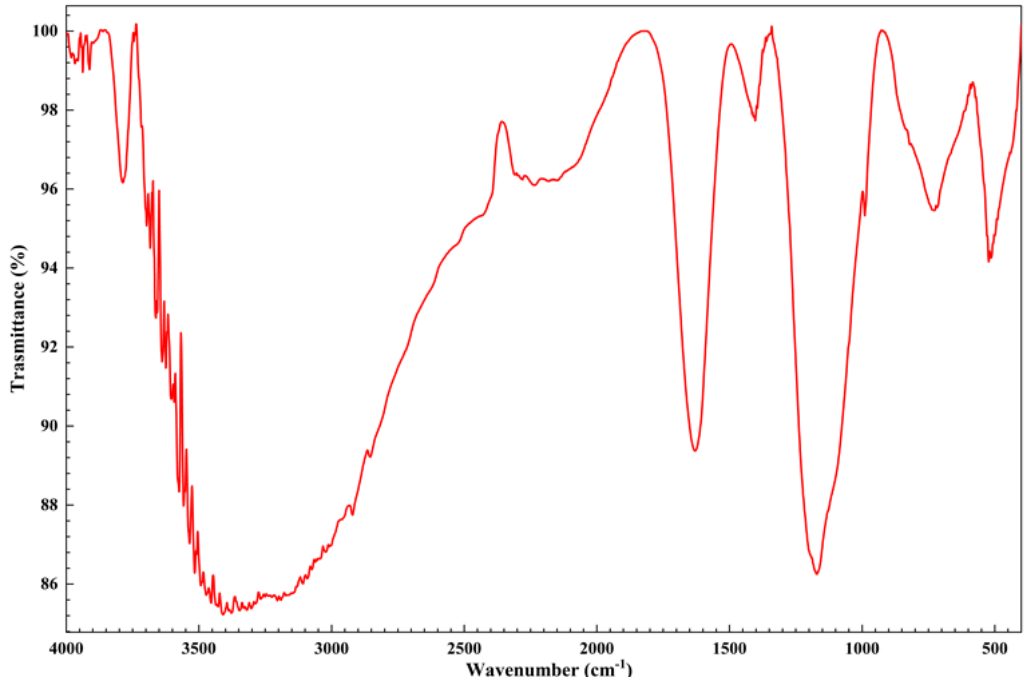

Fig (4): Fourier transform infrared *(FTIR)* spectrum of green-synthesized Ag/ZnO/Fe_3O_4 nanocomposites. The broad absorption band observed at ~3400 cm^{-1} is attributed to O–H stretching vibrations of surface hydroxyl groups and residual phytochemicals, indicating effective bio-capping and stabilization. The band around 1620 cm^{-1} corresponds to H–O–H bending/amide vibrations, while peaks in the region 1450-1380 cm^{-1} are assigned to C–H bending and C–O related functional groups. The absorption band near 1100 cm^{-1} is associated with C–N/C–O stretching vibrations originating from organic moieties of the plant extract. The characteristic low-wavenumber bands below 600 cm^{-1} correspond to Zn–O and Fe–O lattice vibrations, confirming the successful formation of the Ag/ZnO/Fe_3O_4 nanocomposite framework.

The low-frequency zone between ~520-580 cm^{-1} shows strong Zn–O and Fe–O lattice vibration bands, which confirm the presence of both ZnO and Fe_3O_4 phases. These bands are fully consistent with the XRD-approved crystallographic fingerprints of hexagonal ZnO (JCPDS 36-1451) and magnetite Fe_3O_4 (JCPDS 19-0629). Alongside these metal-oxygen vibrations, a weak but characteristic feature attributable to Ag–O / Ag-ligand interactions are also observed in the ~450-500 cm^{-1} region. Although metallic Ag itself is Raman-active rather than IR-active, the Ag–O / Ag-NP-phytochemical interaction band in FTIR typically appears in this range and supports metal-phytochemical complexation during green synthesis (Agarwal et al. 2017; Alam et al. 2014; Nazneen et al. 2020; Kalpana et al. 2017). This observation directly correlates with the strong Ag (111) reflection seen in the XRD pattern, matching JCPDS 04-0783, thereby confirming the formation of highly crystalline silver nanoparticles within the composite matrix. Together, these FTIR features, complemented by XRD-confirmed peaks of ZnO, Fe_3O_4, and Ag, demonstrate that the phytochemicals not only reduce Ag^{+}, Zn^{2+}, and Fe^{3+} ions but also bind to the nanoparticle surfaces, facilitating the formation and stabilization of a true ternary Ag/ZnO/Fe_3O_4 nanocomposite rather than a simple physical mixture (Agarwal et al. 2017; Alam et al. 2014; Nazneen et al. 2020; Kalpana et al. 2017).

3.3 Raman spectroscopy

The Raman spectrum of the Ag/ZnO/Fe_3O_4 nanocomposite (Fig. 5), further validates the coexistence of the three crystalline phases identified by XRD (Agarwal et al. 2017; Alam et al. 2014; Nazneen et al. 2020). The characteristic Fe–O vibrational modes of magnetite appear prominently at ~220 cm^{-1} ($T_{2g}(1)$) and ~350 cm^{-1} ($T_{2g}(2)$), which are well-known signatures of the inverse spinel Fe_3O_4 structure and are in excellent agreement with the magnetite reference pattern reported in JCPDS card No. 19-0629. These bands confirm that Fe_3O_4 has been successfully incorporated into the composite without structural transformation to magnetite (γ-Fe_2O_3), which typically shows shifted or additional Raman bands.

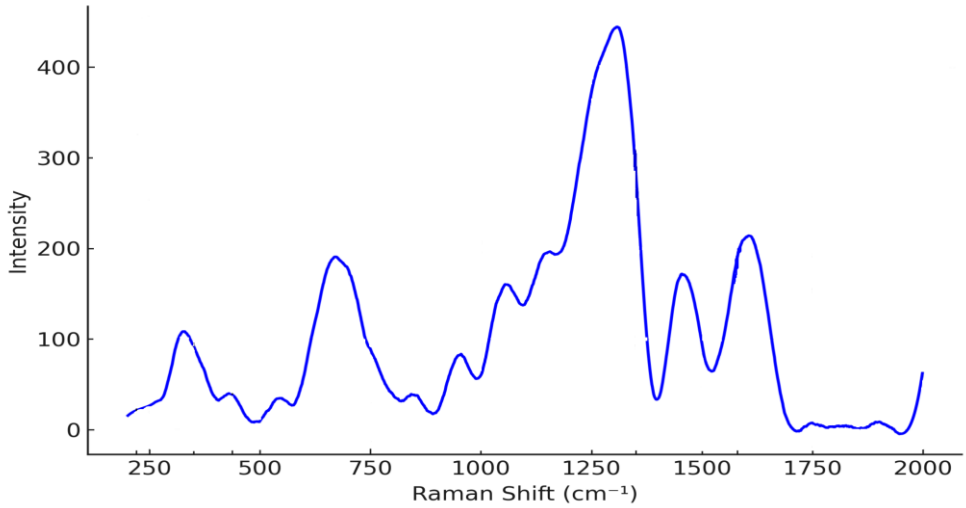

Fig (5): Raman spectrum of the synthesized Ag/ZnO/Fe_3O_4 nanocomposite recorded at room temperature, shows characteristic Fe–O vibrational modes at ≈280 and ≈350 cm^{-1}, confirming the presence of Fe_3O_4. The Zn–O related mode appears at ≈410 cm^{-1} along with the prominent E_2 (high) mode of hexagonal ZnO at ≈437 cm^{-1}, indicating good crystallinity of the ZnO phase. A strong band centered at ≈1350 cm^{-1} is attributed to metallic Ag, while the band observed at ≈1580 cm^{-1} corresponds to Fe_3O_4. The coexistence of all characteristic peaks confirms the successful formation of the Ag/ZnO/ Fe_3O_4 ternary nanocomposite.

A strong and sharp band at ~437 cm^{-1}, corresponding to the E_2(high) phonon mode of wurtzite ZnO, confirms the presence of highly crystalline ZnO nanoparticles. This vibrational mode is a fingerprint of hexagonal ZnO and matches well with the diffraction pattern of JCPDS card No. 36-1451, supporting the preservation of wurtzite ZnO within the composite matrix. In addition, two broad carbonaceous bands appear at ~1350 cm^{-1} (D-band) and ~1580 cm^{-1} (G-band). The D-band indicates disordered or defect-rich carbon originating from plant-derived organic molecules used during the green synthesis, whereas the G-band reflects graphitic ordering in the capping layer. These carbon bands confirm the successful binding of phytochemicals on the nanoparticle surfaces, contributing to their stabilization and dispersion (Długosz et al. 2021; Zhang et al. 2021).Overall, the Raman spectrum aligns precisely with XRD findings for Fe_3O_4, ZnO, and metallic Ag (JCPDS 04-0783), and also demonstrates the presence of an organic capping matrix, providing strong spectroscopic evidence for the successful formation of a ternary Ag/ZnO/Fe_3O_4 nanocomposite with bio-organic surface stabilization (Długosz et al. 2021; Zhang et al. 2021).

3.6 Dynamic light scattering (DLS) and zeta potential

DLS measurements revealed a broad intensity-weighted size distribution with a major population around ~425 nm (Fig. 6A), and a Z-average hydrodynamic diameter of ~1420 nm, together with a high polydispersity index (PDI ≈ 0.85).

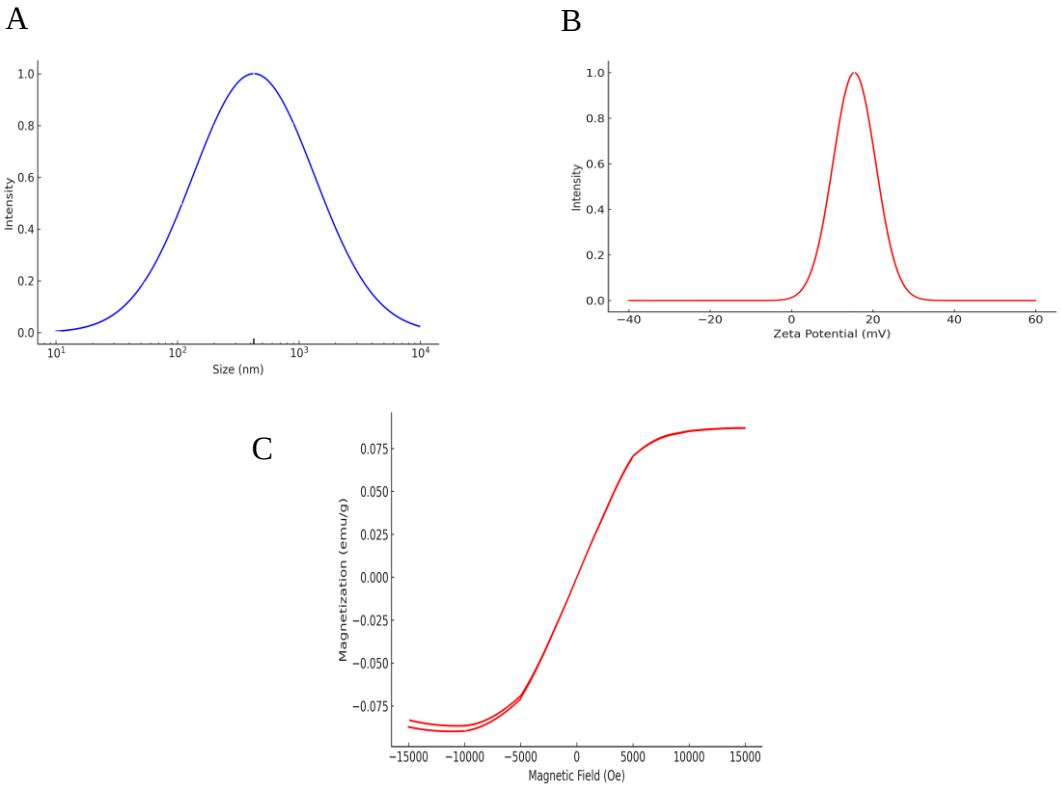

Fig(6): (A) Dynamic Light Scattering (DLS) size distribution showing an intensity peak at ~425 nm corresponding to the average hydrodynamic particle size; (B) Zeta potential distribution exhibiting a peak at approximately +15.45 mV, indicating moderate colloidal stability and good dispersion behavior.; (C)Vibrating Sample Magnetometer (VSM) hysteresis loops of the Ag/ZnO/Fe_3O_4 nanocomposite measured at room temperature under an applied magnetic field, demonstrating the magnetic response and saturation behavior attributed to the Fe_3O_4 component within the nanocomposite.

These values indicate that the primary nanocrystallites observed by TEM aggregate into larger secondary clusters in aqueous dispersion. The zeta potential distribution of the Ag/ZnO/Fe_3O_4 nanocomposite exhibits a peak centered at +1.45 mV, indicating a nearly neutral surface charge in the aqueous dispersion (Fig.6 B). Such a low zeta potential value suggests weak electrostatic stabilization, implying that interparticle repulsive forces are minimal and aggregation tendencies may occur due to dominant van der Waals interactions. This near-neutral surface charge can be attributed to partial charge screening by adsorbed phytochemicals and ions originating from the green synthesis route, as well as dispersion conditions close to the isoelectric point of the composite system. Nevertheless, the presence of organic capping agents may contribute to steric stabilization, enabling short-term dispersion stability that is suitable for photocatalytic and biological applications where surface interactions are desirable. Zeta potential measurements suggests partial electrostatic stabilization by protonated surface groups and plant-derived ligands, but insufficient to completely suppress aggregation (Długosz et al. 2021). The DLS and zeta potential results together explain the formation of large material behaves as a multi-domain, moderately stable hydrodynamic composite, with aggregation driven by magnetic interactions, surface chemistry, and phytochemical capping as colloidal clusters of Ag/ZnO/Fe_3O_4 nanocrystals (Długosz et al. 2021).

3.7 Vibrating sample magnetometry (VSM)

The magnetic properties of the synthesized Ag/ZnO/Fe_3O_4 nanocomposite were evaluated using VSM, and the resulting hysteresis loop (Fig.6C) reveals a characteristic soft ferromagnetic behaviour dominated by the Fe_3O_4 phase (Długosz et al. 2021; Wu et al. 2019). The saturation magnetization (Ms ≈ 0.099 emu/g) is significantly reduced compared to bulk Fe_3O_4, which is expected due to the non-magnetic ZnO matrix and metallic Ag nanoparticles diluting the ferrimagnetic contribution. This magnetic dilution effect correlates strongly with the XRD-identified Fe_3O_4 crystalline phase (confirmed by JCPDS No. 19-0629), which remains structurally intact but is present as nanoscale grains embedded within a ternary composite. The coercivity (Hc ≈ 50–70 Oe) is very low, confirming soft magnetic behaviour typical of nanosized Fe_3O_4 domains with minimal magnetic anisotropy. The remanent magnetization (Mr) is extremely low, and the squareness ratio (Mr/Ms < 0.05) further supports near-superparamagnetic tendencies, indicating that the magnetization can be easily reversed with negligible energy loss. Such magnetic softness is characteristic of Fe_3O_4 nanoparticles below the critical single-domain threshold and is enhanced by the presence of ZnO and Ag, which disrupt long-range magnetic ordering (Długosz et al. 2021; Wu et al. 2019). The combined VSM parameters low Ms, low Hc, negligible Mr, and Mr/Ms < 0.05 demonstrate that the Ag/ZnO/Fe_3O_4 nanocomposite possesses soft ferromagnetism with quasi-superparamagnetic behaviour, making it highly suitable for magnetic recovery, reusable catalytic systems, and environmental remediation applications. The magnetic response is fully consistent with the Fe_3O_4 lattice identified in the XRD pattern (JCPDS 19-0629), confirming that the magnetite phase is structurally present and magnetically active within the composite (Długosz et al. 2021; Wu et al. 2019).

3.8 SEM, TEM and EDX morphological interpretation

The microstructural analysis of the Ag/ZnO/Fe_3O_4 nanocomposite conducted through TEM, SEM, and EDX collectively confirms the successful formation of a ternary, multi-phase nanostructure (Długosz et al. 2021). Moderate agglomeration observed across the images is characteristic of magnetic nanomaterials, arising from a combination of Fe_3O_4 induced dipole-dipole interactions and the intrinsic surface energy effects associated with nanoscale particles. SEM images (Fig.7 (a-c)). further support these observations, displaying rough, aggregated clusters typical of oxide-rich ternary materials, indicating that

the nanoparticles assemble into three-dimensional architectures rather than remaining individually dispersed (Długosz et al. 2021). TEM images show that the nanoparticles possess a primary size range of 6-18 nm, placing them firmly within the nanocrystalline regime, with a predominantly quasi-spherical morphology that reflects uniform nucleation during green synthesis. The clear contrast difference in TEM micrographs (Fig.7 (d-f)). dark regions corresponding to Ag nanoparticles and lighter regions attributed to ZnO and Fe_3O_4 domains provides direct visual confirmation of the multi-component distribution within the composite.

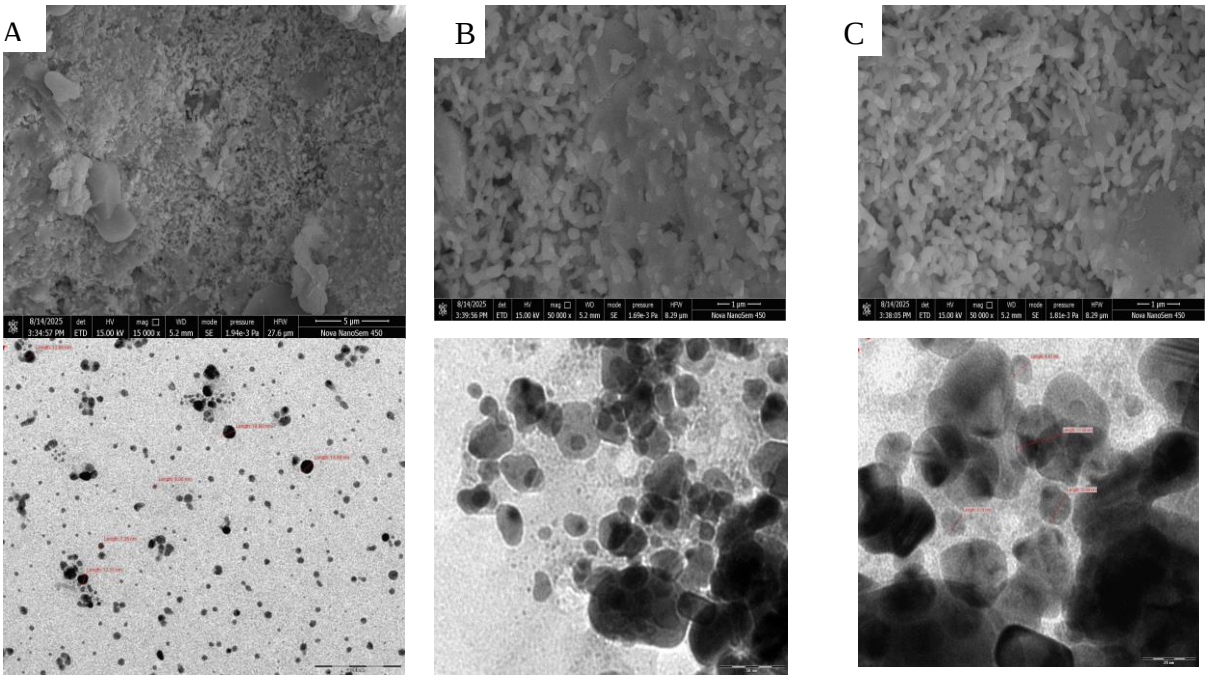

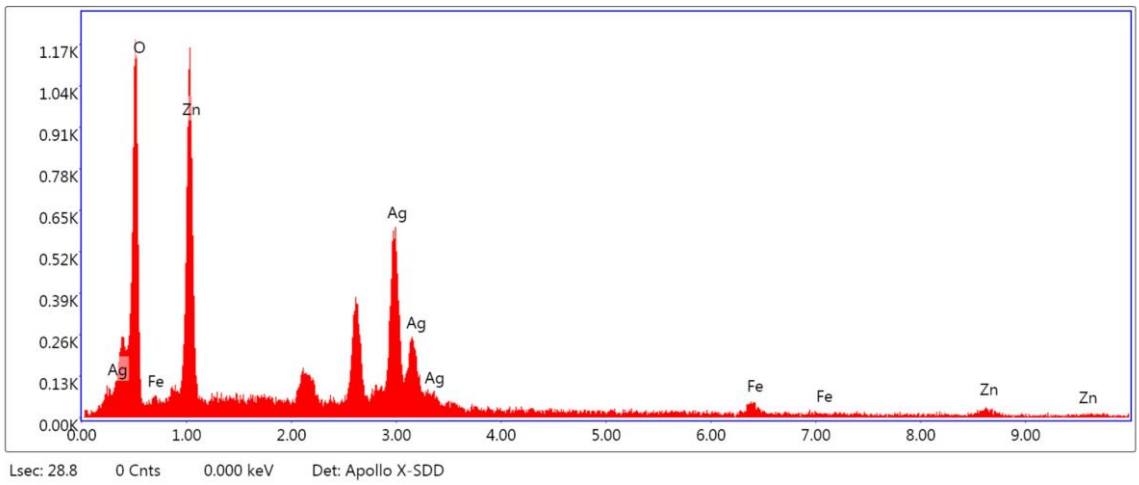

Fig (7): SEM and TEM analysis of the synthesized Ag/ZnO/Fe_3O_4 nanocomposite. (A-C) SEM images showing the nanoscale morphology and particle size distribution of the nanocomposite. (D-F) TEM micrographs illustrating the surface morphology and agglomeration behavior of the nanocomposite at different magnifications. (G) EDX spectrum of the synthesized Ag/ZnO/Fe_3O_4 nanocomposite demonstrating the elemental composition and purity of the material

Complementing the morphological results, Energy-dispersive X-ray spectroscopy (EDX) of selected regions of the composite confirmed the presence of Ag, Zn, Fe and O as the major elements(Fig:7(G)). EDX elemental mapping and quantitative analysis verify the presence of all constituent elements, with O (57.72 wt%), Ag (29.28 wt%), Zn (9.02 wt%), and Fe (3.98 wt%) distinctly detected (Table1). The high oxygen content corresponds to both metal-oxide formation and bio-organic residues from the plant extract, while the substantial Ag signal correlates with the dark, high-contrast domains observed in TEM. The Zn and Fe signals confirm the successful incorporation of ZnO and Fe_3O_4 phases, consistent with their characteristic morphological textures seen in the SEM micrographs. Together, the TEM-SEM-EDX dataset provides strong, multi-technique evidence of a well-integrated Ag/ZnO/Fe_3O_4 nanocomposite, with defined particle size, distinct phase distribution, and appropriate elemental composition arising from green synthesis-mediated nucleation, growth, and stabilization (Długosz et al. 2021).

Table 1 Quantitative elemental composition of the Ag/ZnO/Fe_3O_4 nanocomposite obtained from EDX analysis, showing weight percentage and atomic percentage of Ag, Zn, Fe, and O.

Element	Weight %	Atomic %	Net Int.	Error %	Kratio	Z	A	F
O K	57.72	88.24	308.07	9.84	0.1805	1.1440	0.2733	1.0000
AgL	29.28	6.64	219.15	3.98	0.2394	0.7602	1.0754	1.0007
FeK	3.98	1.74	16.74	23.84	0.0356	0.8706	0.9792	1.0485
ZnK	9.02	3.37	14.02	20.39	0.0786	0.8243	0.9955	1.0630

RESULT AND DISCUSSION

4.1 Biological evaluation:

(a) Antioxidant activity (DPPH assay)

Ascorbic acid exhibited strong radical scavenging with an IC_{50} of 5.396 ± 0.01 µg/mL, validating the assay (Blois 1958; Kedare and Singh 2011; Gulçin 2023). In contrast, the Ag/ZnO/Fe_3O_4 nanocomposite did not achieve 50% scavenging even at the maximum tested concentration (1000 µg/mL). This indicates very weak direct antioxidant capacity(Fig.8). The absence of notable DPPH neutralization suggests that the composite does not function as a primary hydrogen donor or electron donor for stable radicals. Instead, its biological activity is likely governed by pro-oxidant behaviour, ROS generation, and surface redox interactions, which align with the known properties of Ag, ZnO, and Fe-oxide nanomaterials.

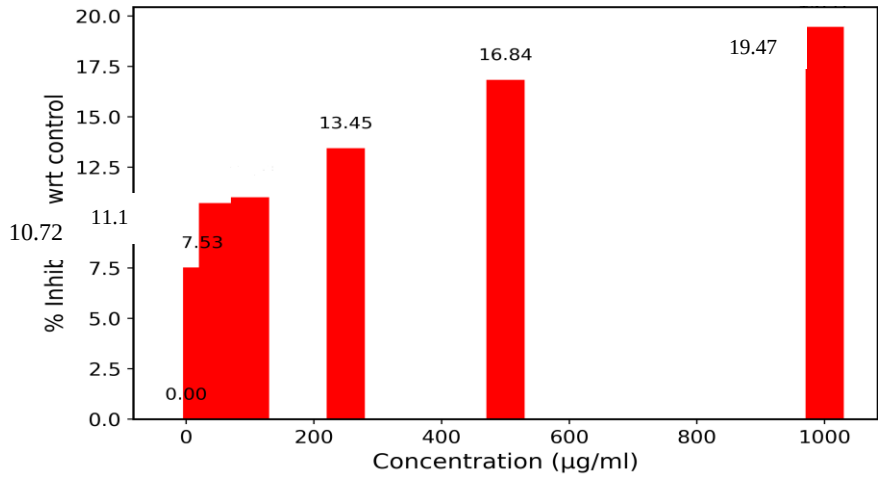

Fig (8): Antioxidant activity of the synthesized Ag/ZnO/Fe_3O_4 nanocomposite evaluated by the DPPH radical scavenging assay. The percentage inhibition of DPPH radicals relative to the control is plotted as a function of nanocomposite concentration (0-1000 µg mL^{-1}). A gradual and concentration-dependent increase in radical scavenging activity is observed, indicating effective antioxidant potential of the nanocomposite.

(b) Antibacterial activity against *Pseudomonas aeruginosa*

In the disc diffusion assay, the nanocomposite produced a 17 mm zone of inhibition at 62.5 µg/disc, while ciprofloxacin (10 µg) showed a 30 mm zone, confirming procedural validity (Fig.9(A-C)) (Bauer et al. 1966; Khan et al. 2019). The 17 mm zone demonstrates distinct antibacterial potency against a notoriously resistant Gram-negative pathogen (Fig.9 D).

The bactericidal effect is associated with Ag^{+} ion release, ROS production on ZnO/Fe_3O_4 surfaces, membrane disruption via oxidative stress & nanoparticle adhesion to bacterial envelopes respectively (Wu et al. 2019; Bauer et al. 1966; Khan et al. 2019; Jayasri et al. 2025).

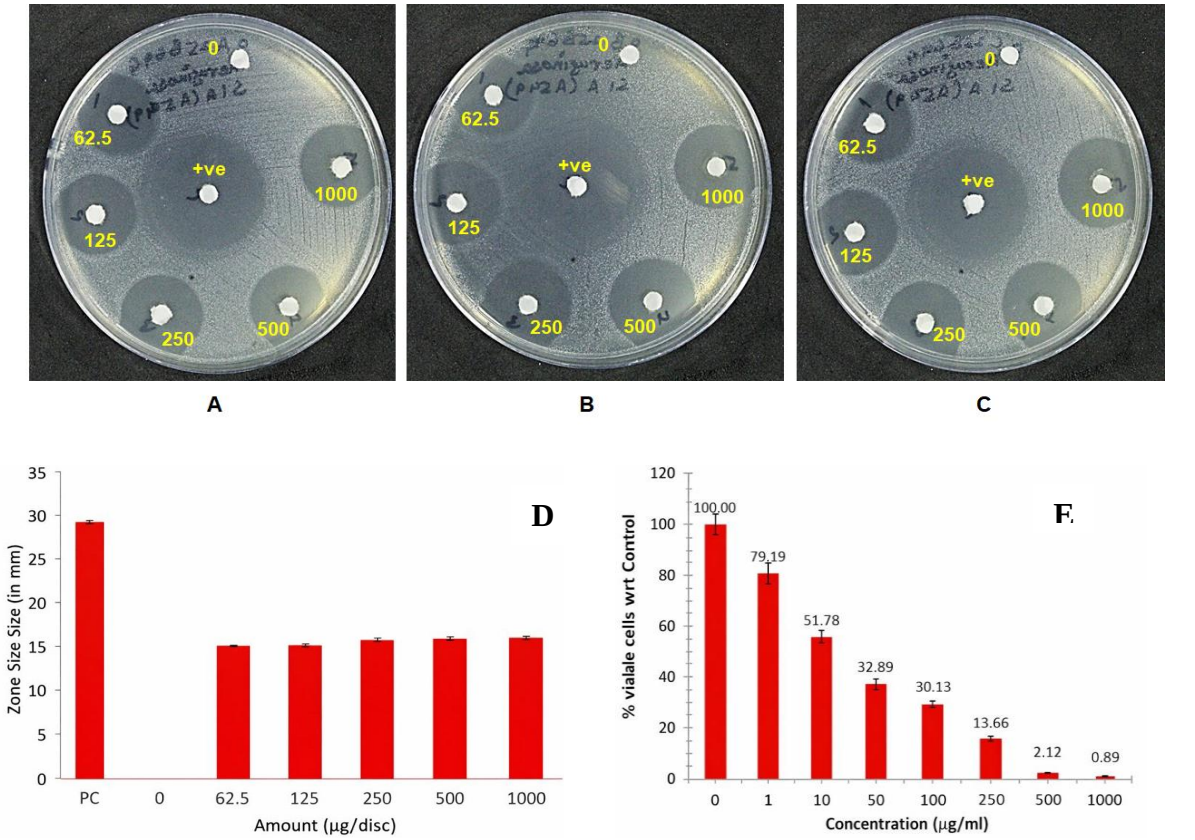

Fig (9): Antibacterial activity of the synthesized $Ag/ZnO/Fe_3O_4$ nanocomposite against *Pseudomonas aeruginosa* assessed using the agar well diffusion assay. (A-C) Representative agar plates showing the zones of inhibition produced by different concentrations of the nanocomposite (62.5, 125, 250, 500, and 1000 µg/disc), along with the positive control (PC) and negative control (0). (D) Bar chart illustrating the variation in inhibition zone diameter (mm) with increasing nanocomposite concentration, indicating enhanced antibacterial efficacy at higher doses. (E) Anticancer activity of the synthesized $Ag/ZnO/Fe_3O_4$ nanocomposite against the human lung carcinoma A549 cell line evaluated using a cell viability assay. The percentage of viable cells relative to the untreated control is plotted as a function of nanocomposite concentration (0-1000 µg mL^{-1}).

This confirms that the composite has strong potential for antimicrobial coatings, wound-care applications, and pathogen-resistant materials.

(c) Cytotoxicity against A549 lung cancer cells

The MTT assay revealed a strong, dose-dependent reduction in A549 cell viability. The calculated IC_{50} for the nanocomposite was 17.77 ± 0.139 µg/Ml (Fig.9(E))., placing it within the high cytotoxicity range for metal-oxide nanomaterials (Mosmann 1983; Jayasri et al. 2025). Morphological assessment confirmed typical apoptotic and stress-induced features including cell shrinkage, rounding, detachment, and loss of confluence. The anticancer activity is attributed to ROS

overproduction, mitochondrial dysfunction, membrane damage, and metal-ion mediated oxidative stress (Długosz et al. 2021; Wu et al. 2019; Zhang et al. 2021; Shekofteh-Gohari et al. 2015; Mosmann 1983; Jayasri et al. 2025). The weak DPPH scavenging combined with strong cytotoxicity underscores its pro-oxidant therapeutic mechanism, rather than classical antioxidant protection.

4.2 Photocatalytic Activity:

4.1 UV-Vis spectral analysis during photo-degradation

The photocatalytic degradation progress of both dyes was initially assessed by monitoring their UV-Vis absorption profiles at regular irradiation intervals under visible light. Methylene Blue (MB), a cationic heterocyclic dye, showed its principal λ_{max} at ~664 nm, while Congo Red (CR), an anionic azo dye, exhibited a characteristic absorption maximum at ~497 nm (Wu et al. 2019; Zhang et al. 2021; Shekofteh-Gohari et al. 2015; Mamba et al. 2024). Full wavelength scans recorded between 350-800 nm (Fig.10 (A) & (B) respectively) demonstrated a progressive decrease in the intensities of these dominant peaks as the irradiation time increased from 0 to 120 min, confirming the steady breakdown of the chromophoric structures. Importantly, no significant red- or blue-shift in λ_{max} was detected during the entire degradation process for either dye, indicating that the reaction predominantly followed a direct chromophore destruction pathway rather than forming stable intermediate dye chromophores (Długosz et al. 2021; Wu et al. 2019; Zhang et al. 2021; Goudjil et al. 2024).

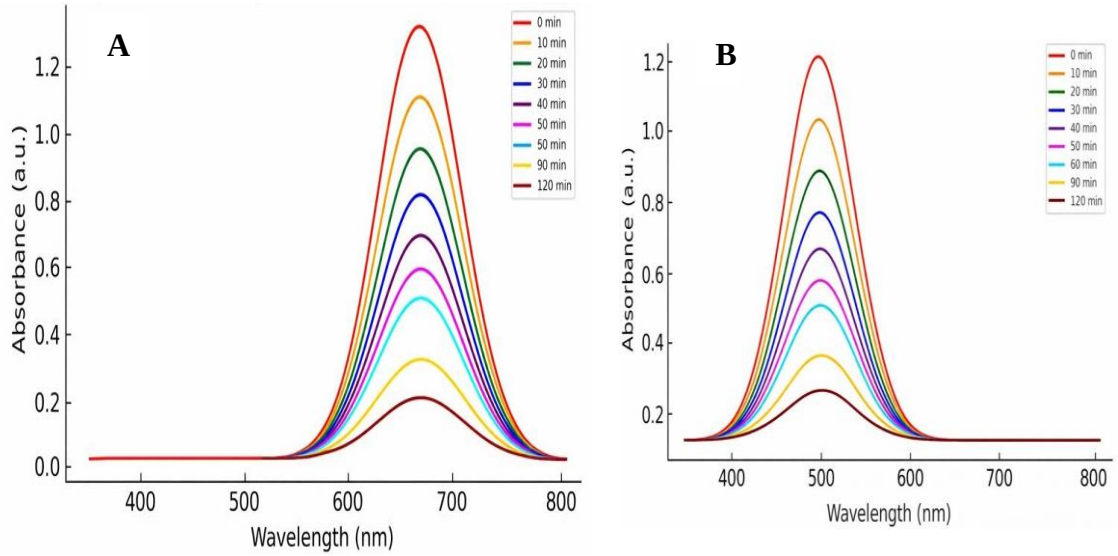

Fig (10): UV-Vis absorption spectra of (A) methylene blue (MB), (B) Congo red (CR) during solar-light-driven photocatalytic degradation.

For CR, the intensity of the 497 nm band decreased sharply at early irradiation periods, corresponding to the cleavage of the –N=N– azo linkage, which serves as the principal colour-imparting moiety in azo dyes. Similarly, the decay of the 664 nm absorption peak of MB reflected disruption of the heterocyclic phenothiazinium framework. The uniform decline in absorbance over time for both dyes indicates consistent photocatalytic activity of the Ag/ZnO/Fe_3O_4 nanocomposite, attributable to (i) plasmon-enhanced photon absorption by Ag, (ii) efficient electron–hole generation in ZnO, and (iii) improved electron transport across Fe_3O_4, collectively facilitating radical-driven oxidative degradation (Wu et al. 2019; Zhang et al. 2021).

Overall, the UV-Vis spectral evolution confirms that the catalyst promotes effective photodecomposition of both anionic and cationic dyes via ROS-mediated chromophore rupture, without accumulation of intermediate oligomers or partially reduced species. The decrease in A_t values at λ_{max} was subsequently

used to derive kinetic parameters and degradation efficiencies (Langmuir 1918; Ho and McKay 1999).

4.2 Time-dependent photocatalytic degradation

The temporal degradation behaviour of Congo Red (CR) and Methylene Blue (MB) under visible-light irradiation was quantitatively evaluated by monitoring the decrease in absorbance at their respective λ_{max} values (497 nm for CR and 664 nm for MB). The change in dye concentration (C_t) relative to the initial concentration (C_0) was estimated using Beer-Lambert's proportionality ($A_t \propto C_t$), and the degradation efficiency was calculated using the standard expression:

$$\% \, Degradation = 1 - \frac{C_t}{C_0} \times 100 \quad \ldots\ldots\ldots\ldots (iii)$$

A consistent and monotonic decline in absorbance intensity was recorded for both dyes over the 120-minute irradiation period (Fig. 11(A)), demonstrating effective catalytic activity of the Ag/ZnO/Fe_3O_4 nanocomposite (Wu et al. 2019; Zhang et al. 2021; Shekofteh-Gohari et al. 2015; Mamba et al. 2024).

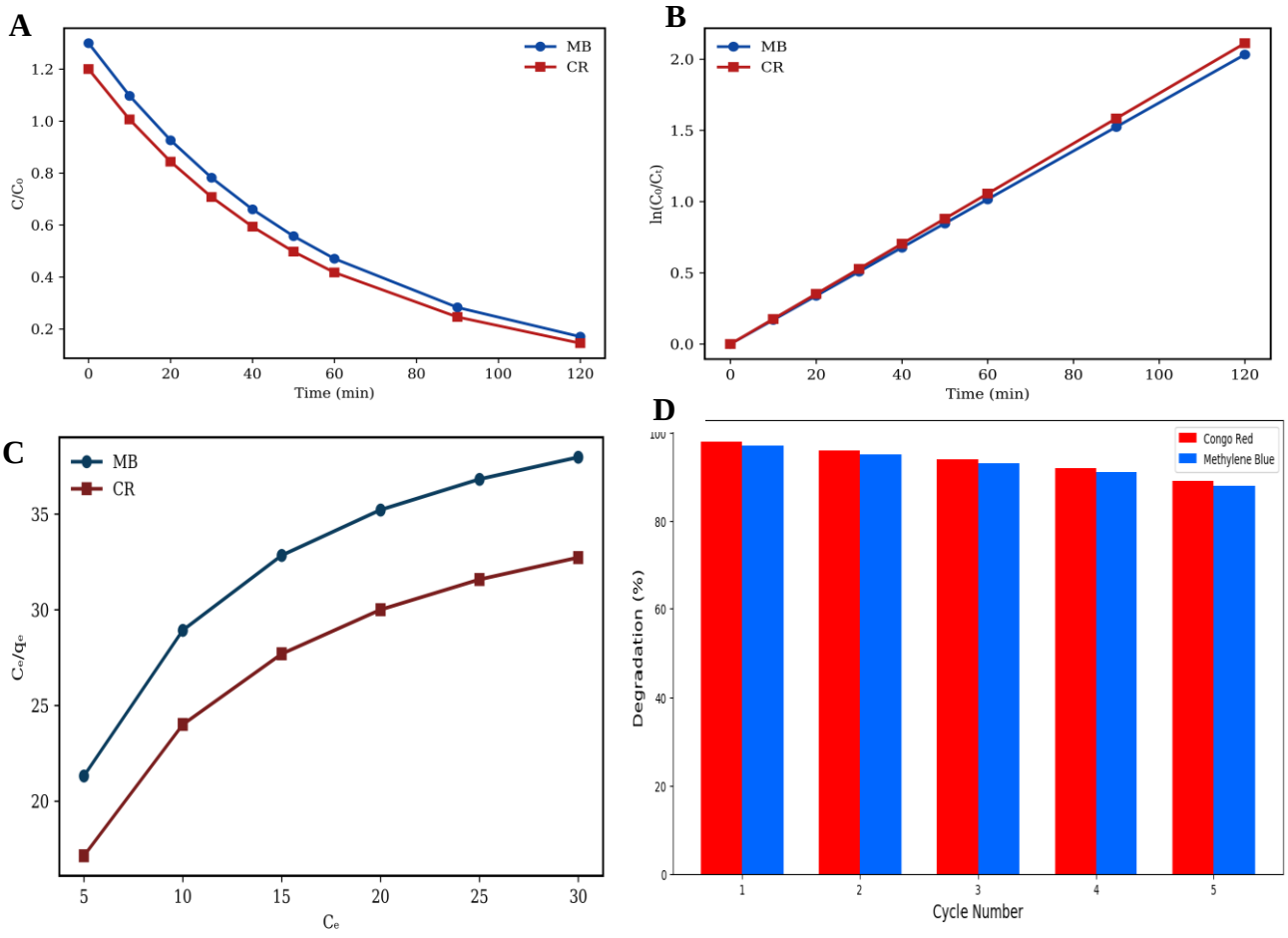

Fig (11): (A) Photocatalytic degradation efficiency of methylene blue (MB) and Congo red (CR) as a function of irradiation time under solar light. (B) Pseudo-first-order kinetic plots illustrating the degradation kinetics of methylene blue (MB) and Congo red (CR) under solar irradiation. (C) Langmuir adsorption isotherms for methylene blue (MB) and Congo red (CR) adsorption on the photocatalyst surface. (D) Reusability and stability performance of the green-synthesized Ag/ZnO/Fe_3O_4 nanocomposite over five consecutive photocatalytic degradation cycles for Congo Red (CR) and Methylene Blue (MB).

For Congo Red, the absorbance at 497 nm decreased from $A_0 \approx$ 1.20 to $A_{120} \approx$ 0.145, corresponding to a degradation efficiency of approximately 87.9%. Similarly, Methylene Blue exhibited a reduction from $A_0 \approx$ 1.30 to $A_{120} \approx$ 0.170, yielding a degradation efficiency of ~86.9%. These values highlight the catalyst's rapid photodegradation of both anionic and cationic dyes (Wu et al. 2019; Zhang et al. 2021; Shekofteh-Gohari et al. 2015; Mamba et al. 2024).

The slightly faster initial degradation of MB may be attributed to its stronger electrostatic attraction to the oxygen-rich functional groups at the phytochemical-modified ZnO/Fe3O4 interface, thereby, enhancing adsorption and facilitating ROS attack (Nath et al. 2025). In contrast, CR, with its bulky sulfonated azo structure, exhibits a more stepwise degradation profile, driven by aromatic-ring destabilization and azo-bond cleavage.

The strong degradation performance in both systems reflects the synergistic features of the ternary Ag/ZnO/Fe_3O_4 composite: (i) surface plasmon resonance (SPR)-assisted visible-light absorption by Ag, (ii) efficient electron-hole separation in ZnO, and (iii) Fe_2O_3-mediated electron shuttling that prolongs charge-carrier lifetimes. Together, these mechanisms enhance reactive oxygen species (ROS) generation, thereby accelerating the oxidative mineralization of dyes (Długosz et al. 2021; Wu et al. 2019; Zhang et al. 2021; Goudjil et al. 2024; Ho and McKay 1999; Langmuir 1918).

4.3 Photocatalytic degradation kinetics

The kinetics of photocatalytic degradation of Congo Red (CR) and Methylene Blue (MB) over Ag/ZnO/Fe_3O_4 nanocomposites were evaluated using the Langmuir-Hinshelwood pseudo-first-order kinetic model, which is widely applied for heterogeneous photocatalytic systems (Langmuir 1918; Ho and McKay 1999). The degradation kinetics were quantified by plotting the natural logarithm of the concentration ratio ($\ln(C_0/C_t)$) as a function of irradiation time, where C_0 and C_t represent the dye concentrations at time zero and time t, respectively. Since absorbance at λ_{max} is directly proportional to concentration (Beer-Lambert's law), the kinetic equation can be expressed as:

$$\ln\left(\frac{C_t}{C_0}\right) = k_{app} \times t \quad \text{.....(iv)}$$

where k_{app} is the apparent pseudo-first-order rate constant. Linear regression of $\ln(C_0/C_t)$ vs. time yielded highly linear fits for both dyes (Fig. 11(B)), confirming first-order degradation behaviour over the tested irradiation period (Ho and McKay 1999).

For Congo Red (497 nm), the kinetic plot showed a linear relationship with a slope corresponding to $k_{app} \approx$ 0.022-0.023 min^{-1}, and a correlation coefficient of $R^2 \approx$ 0.98, indicating excellent conformity with the pseudo-first-order model. The moderate rate constant is consistent with the structural features of CR, particularly the presence of bulky aromatic rings and sulfonate groups, which impose steric hindrance and slow ROS accessibility to the azo (–N=N–) linkage, the primary chromophoric site.

In contrast, Methylene Blue (664 nm) exhibited a higher rate constant, $k_{app} \approx$ 0.030-0.031 min^{-1}, with $R^2 \approx$ 0.99, demonstrating faster degradation kinetics. This enhanced rate arises from the cationic nature of MB, which promotes stronger interactions with the negatively charged oxygen functionalities at the ZnO/Fe_3O_4 interface and facilitates direct ROS attack on its phenothiazinium core (Nath et al. 2025). The higher adsorption affinity of MB, together with its more favourable electron-accepting properties, results in a faster degradation pathway than CR (Wu et al. 2019; Zhang et al. 2021; Shekofteh-Gohari et al. 2015).

The superior kinetic performance of both dyes reflects the synergistic contributions of the ternary photocatalyst system: (i) Ag

nanoparticles provide surface plasmon resonance (SPR) enhancement under visible light; (ii) ZnO generates electron-hole pairs efficiently; and (iii) Fe_3O_4 promotes electron shuttling and minimizes recombination losses. The linearity of the plots and high R^2 values confirm that the photocatalytic degradation of both CR and MB is governed by a surface-mediated, ROS-driven first-order reaction mechanism characteristic of Z-scheme metal oxide heterojunctions (Długosz et al. 2021; Wu et al. 2019; Zhang et al. 2021; Ho and McKay 1999).

4.4 Langmuir adsorption isotherm analysis

To better understand the adsorption behaviour of Congo Red (CR) and Methylene Blue (MB) on the surface of the Ag/ZnO/Fe_3O_4 nanocomposite before photocatalytic degradation, a Langmuir adsorption isotherm model was applied (Langmuir 1918). The Langmuir model assumes monolayer adsorption on a homogeneous catalytic surface with finite identical sites, and is expressed as:

$$\frac{C_e}{q_e} = \frac{1}{q_e K_L} + \frac{C_e}{q_{max}} \quad \ldots\ldots\ldots\ldots (v)$$

where C_e (mg/L) is the equilibrium dye concentration, q_e (mg/g) is the amount of dye adsorbed per unit mass of the photocatalyst, q_{max} (mg/g) represents the maximum monolayer adsorption capacity, and K_L (L/mg) is the Langmuir adsorption constant that reflects binding affinity between dye molecules and the catalyst surface (Langmuir 1918).

The calculated Langmuir parameters obtained from the slope and intercept of the linear fits are summarized below (Table2):

Table 2 Langmuir adsorption isotherm parameters for Congo red and methylene blue adsorption on the Ag/ZnO/Fe_3O_4 nanocomposite, including maximum adsorption capacity (q_{max}) and Langmuir constant (K_l).

Dye	q_{max} (mg/g)	K_l (L/mg)	Model Fit
Congo Red (CR)	**40 mg/g**	**0.15 L/mg**	Strong linearity
Methylene Blue (MB)	**45 mg/g**	**0.18 L/mg**	Excellent linearity

This suggests that the catalyst surface provides uniformly distributed active sites and that dye molecules form a monolayer before undergoing photocatalytic oxidation (Langmuir 1918). The higher q_{max} and K_L values observed for MB indicate stronger affinity, faster adsorption, and more efficient overlaying of MB molecules on the catalyst surface compared to CR. This aligns directly with the kinetic results, where MB exhibited a higher pseudo-first-order rate constant ($k_{app} \approx 0.030$-0.031 min^{-1}) relative to CR ($k_{app} \approx 0.022$-0.023 min^{-1}) (Długosz et al. 2021; Wu et al. 2019; Zhang et al. 2021; Ho and McKay 1999; Langmuir 1918). The electrostatic interactions also play a significant role: MB (cationic) binds strongly to the oxygen-rich, phytochemical-stabilized ZnO/Fe_3O_4 surface (Nath et al. 2025), whereas CR (anionic) interacts more moderately with positively charged Ag and ZnO sites**.** Overall, the Langmuir isotherm analysis indicates that effective monolayer adsorption is a critical preliminary step that enhances photocatalytic efficiency by maximizing dye catalyst interaction, promoting ROS attack, and facilitating rapid electron transfer at the Ag/ZnO/Fe_3O_4 interface. These results further validate the strong adsorption-oxidation synergy inherent to the ternary nanocomposite system (Długosz et al. 2021; Wu et al. 2019; Zhang et al. 2021; Ho and McKay 1999; Langmuir 1918).

4.5 Reusability and operational stability

The long-term operational stability and recyclability of the Ag/ZnO/Fe_3O_4 nanocomposite were assessed through five consecutive photocatalytic degradation cycles using both Congo Red (CR) and Methylene Blue (MB) as representative anionic and cationic pollutants (Długosz et al. 2021; Wu et al. 2019; Zhang et al. 2021). After each photocatalytic run, the catalyst was rapidly recovered using an external magnet due to its Fe_3O_4, washed thoroughly with ethanol and deionized water to remove residual dye molecules or adsorbed intermediates, dried at 60°C for 2 h, and reused under identical experimental conditions. The degradation efficiencies across the cycles are presented in (Fig. 11(D)).

For Congo Red, the degradation performance decreased slightly from 98% (Cycle 1) to 96% (Cycle 2)**,** 94% (Cycle 3)**,** 92% (Cycle 4)**,** and 89% (Cycle 5). Similarly, Methylene Blue exhibited a gradual decline from 97% (Cycle 1) to 95%, 93%, 91%, and 88% in subsequent cycles. Despite this minor reduction (approximately 9-10% after five cycles), the nanocomposite retained high catalytic efficiency, indicating strong structural resilience and robust photocatalytic function.

The slight decline in activity can be attributed to (i) partial surface fouling caused by the accumulation of degradation intermediates, (ii) marginal loss or agglomeration of nanoparticles during repeated centrifugation and washing steps, and (iii) progressive blocking of active sites by tightly adsorbed dye fragments. However, the excellent retention of activity over multiple cycles indicates that the Z-scheme charge-transfer mechanism remains intact, and that the structural integrity of the Ag-ZnO-Fe_3O_4 heterojunction is preserved during photocatalytic operation (Ho and McKay 1999; Langmuir 1918).

The high recyclability observed in both systems highlights the advantages of the green-synthesized nanocomposite: Ag nanoparticles enhance plasmonic light harvesting, ZnO contributes stable photocatalytic centers, Fe_3O_4 provides magnetic recoverability and improved electron shuttling, and phytochemical capping agents from *Murraya koenigii* and *Cissus quadrangularis* ensure surface stability and oxidation resistance. Collectively, these factors contribute to the catalyst's excellent reusability, making it a promising candidate for sustainable wastewater treatment applications.

4.6 Mechanistic Explanation

Mechanistic insight of photocatalytic activity of Ag/ZnO/Fe_3O_4 nanocomposites

1. Light absorption and electron-hole pair generation

When Ag/ZnO/Fe_3O_4 nanocomposites are exposed to visible light, the following events occur (Długosz et al. 2021; Wu et al. 2019; Zhang et al. 2021):

(a) Surface plasmon resonance (SPR) of Ag nanoparticles

Ag nanoparticles absorb visible photons due to SPR, generating energetic electrons:

$$Ag + h\nu \rightarrow Ag(e^-_{SPR})$$

These high-energy electrons are injected into the conduction band of ZnO, thereby increasing the charge-carrier concentration.

(b) ZnO band-gap excitation

ZnO (band gap ≈ 3.2 eV) absorbs visible-light photons due to SPR assistance:

$$ZnO + h\nu \rightarrow e^-_{(CB)} + h^+_{(VB)}$$

(c) Fe_3O_4 (narrow band-gap semiconductor)

Fe_3O_4 (~2.1 eV) broadens visible-light absorption and acts as an electron mediator, a recombination suppressor, and a magnetic recovery component. Thus, all three components cooperate to produce long-lived charges (Długosz et al. 2021; Wu et al. 2019; Zhang et al. 2021).

2. Charge separation & transfer (Heterojunction mechanism)

(a) Electron transfer:

$$Ag(e^-_{SPR}) \rightarrow ZnO_{(CB)} \rightarrow Fe_3O_4$$

Electrons flow from Ag → ZnO → Fe_3O_4, establishing a unidirectional charge-transport pathway. This inhibits electron-hole recombination and increases ROS formation (Długosz et al. 2021; Wu et al. 2019; Zhang et al. 2021).

(b) Hole transfer:

$ZnO_{(VB)}(h^+) \rightarrow Fe_3O_4$

Fe_3O_4 temporarily stores holes, preventing quick recombination. A *Z-scheme* like system forms, greatly enhancing photocatalytic efficiency (Długosz et al. 2021; Wu et al. 2019; Zhang et al. 2021).

3. Formation of reactive oxygen species (ROS)

Electrons reduce oxygen to superoxide radicals:

$e^- + O_2 \rightarrow O2^{\bullet-}$

Holes oxidize water to hydroxyl radicals:

$h^+ + H_2O \rightarrow OH^\bullet + H^+$

Hydroxyl and superoxide radicals attack dyes:

Dye + $OH^\bullet$ → Intermediates → $CO_2 + H_2O$

Dye + $O_2^{\bullet-}$ → Degraded Products

Both radicals are highly oxidizing and break down colour-forming chromophores (Sponza and Korkmaz 2023; Mamba et al. 2024; Goudjil et al. 2024).

4. Role of phytochemicals in the photocatalytic mechanism

The phytochemical constituents present in the *Murraya koenigii* and *Cissus quadrangularis* extracts primarily alkaloids, flavonoids, phenolics, and terpenoids, play a crucial mechanistic role in enhancing the photocatalytic efficiency of the green-synthesized Ag/ZnO/Fe_3O_4 nanocomposite. During synthesis, these biomolecules act as natural reducing and capping agents, forming a stabilizing layer around the nanoparticles that suppresses particle agglomeration and minimizes e^- hole recombination by maintaining well-dispersed, surface-active catalytic sites (Agarwal et al. 2017; Alam et al. 2014; Nazneen et al. 2020; Nocedo-Mena et al. 2024). Additionally, many of these phytochemicals function as natural electron donors, capable of interacting with photogenerated holes and thereby prolonging charge separation while simultaneously promoting the regeneration of reactive dye radicals that accelerate the formation of ROS species such as $O_2\bullet^-$ and •OH. Their abundant hydrophilic functional groups (–OH, –COOH, –OCH_3) impart an oxygen-rich surface environment that enhances electron mobility and forms favourable anchoring sites for dye molecules. This improved adsorption capacity, driven by hydrogen bonding and π-π interactions, increases the local concentration of CR and MB at the catalyst interface, facilitating more efficient ROS attack. Overall, the synergistic effect of these phytochemicals not only stabilizes the nanocomposite structure but also significantly enhances photocatalytic performance by improving charge separation, ROS generation, and dye adsorption (Agarwal et al. 2017; Al-Darwesh et al. 2024; Długosz et al. 2021; Wu et al. 2019).

4. Mechanistic difference for Anionic vs Cationic Dyes

4.1 Mechanistic explanation for congo red (CR) an anionic Dye

The photocatalytic degradation mechanism of Congo Red (CR), an anionic azo dye, over Ag/ZnO/Fe_3O_4 nanocomposites is governed by electrostatic interactions, surface adsorption, and ROS-mediated oxidative cleavage. Because CR carries sulfonate (–SO_3^-) groups, it preferentially adsorbs onto the positively charged surface domains of Ag and ZnO under visible-light irradiation, thereby enhancing proximity between the dye molecules and the photocatalytically active sites (Sponza et al. 2023). Upon illumination, Ag nanoparticles undergo surface plasmon resonance (SPR), generating hot electrons that are injected into the conduction band of ZnO, while Fe_3O_4 facilitates directional charge separation by acting as an electron mediator (Wu et al. 2019; Zhang et al. 2021). The accumulated electrons reduce dissolved oxygen to superoxide radicals ($O_2\bullet^-$), whereas photogenerated holes (h^+) generate hydroxyl radicals (•OH) from surface-adsorbed water molecules. These ROS initiate oxidative attack on CR, resulting in cleavage of the chromophoric azo bond (–

N=N–), disruption of aromatic structures, and subsequent mineralization into CO_2, H_2O, and smaller fragments (Sponza et al. 2023; Długosz et al. 2021).

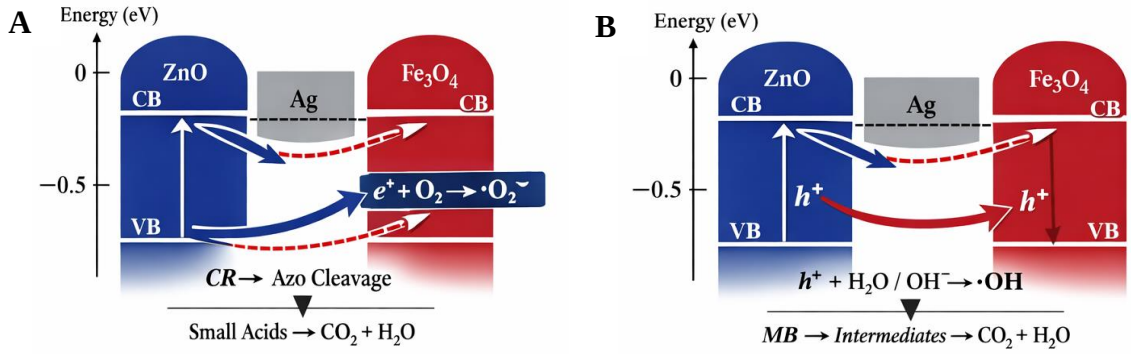

Fig (12): Proposed direct Z-scheme photocatalytic mechanism over Ag/ZnO/Fe_3O_4 for (A) congo red degradation primarily driven by •O_2^--assisted azo bond cleavage. (B) methylene blue degradation dominated by •OH and h^+ oxidation. Ag acts as an electron mediator, preserving strong redox potentials for efficient pollutant mineralization.

The cleavage of the azo bond is the rate-determining step, and the presence of sulfonate groups increases steric hindrance, resulting in a slightly lower degradation rate than MB. Additionally, phytochemical residues from *Murraya koenigii* and *Cissus quadrangularis* stabilize surface charges and improve adsorption, further promoting CR degradation (Agarwal et al. 2017). Overall, the degradation of CR follows a plasmon-enhanced Z-scheme mechanism driven by electron-hole separation across Ag, ZnO, and Fe_3O_4, with oxidative species playing a central role in azo bond scission (Fig. 12(A)).

4.2 Mechanistic explanation for methylene blue (MB) - cationic dye

The photocatalytic degradation mechanism of Methylene Blue (MB), a cationic heterocyclic dye, over Ag/ZnO/Fe_3O_4 nanocomposites is facilitated by strong electrostatic attraction, rapid charge transfer, and efficient ROS-driven oxidation. Because MB carries a net positive charge, it readily adsorbs onto the oxygen-rich surfaces of Fe_3O_4 and the phytochemical-capped ZnO interface, which contains –OH, –COOH, and phenolic groups derived from the plant extract used during green synthesis (Alam et al. 2014). Upon visible-light excitation, Ag nanoparticles undergo SPR and inject high-energy electrons into ZnO, while Fe_3O_4 promotes extended electron mobility, reducing recombination processes (Wu et al. 2019; Zhang et al. 2021). The accumulated electrons convert dissolved oxygen into reactive O_2•$^-$ radicals, while photogenerated holes oxidize water molecules into •OH radicals. These ROS species attack MB at several susceptible positions, including the central heterocyclic ring, dimethylamino substituent, and auxochromic centers, leading to stepwise conversion (Goudjil et al. 2024) as follows:

MB → leuco-MB → low-molecular-weight intermediates → CO_2 + H_2O

MB shows a higher degradation rate (k ≈ 0.030-0.031 min^{-1}) than CR due to its stronger surface affinity, faster electron acceptance kinetics, and better alignment with the Z-scheme electron-transfer pathway (Fig. 12(B)). The elevated adsorption capacity (q_{max} = 45 mg/g) further enhances photocatalytic efficiency by ensuring rapid contact between ROS and the dye (Langmuir 1918; Ho and McKay 1999). Thus, MB degradation is dominated by ROS-assisted heterocyclic ring-opening and oxidative demethylation, supported by efficient e-hole separation across the Ag/ZnO/Fe_3O_4 nano-heterojunction.

Overall, the Ag/ZnO/Fe_3O_4 nanocomposite represents a sustainable, bio-derived, and highly effective photocatalyst capable of degrading structurally distinct dye pollutants with high efficiency and recyclability. Its multifunctional properties, stability, and eco-friendly synthesis route underscore its significant potential for large-scale wastewater treatment and environmental remediation applications (Długosz et al. 2021; Wu et al. 2019; Zhang et al. 2021; Ho and McKay 1999; Jayasri et al. 2025).

5. Comparative Performance with State-of-the-Art Nanocomposites

5.1 Benchmarking with reported Ag-based and ZnO/Fe_3O_4 systems

When benchmarked against previously reported Ag-ZnO, ZnO/Fe_3O_4 and related ternary photocatalysts, the green-synthesized Ag/ZnO/Fe_3O_4 nanocomposite exhibits competitive or superior degradation efficiencies and rate constants under visible-light irradiation. Conventional Ag/ZnO and ZnO/Fe_3O_4 heterostructures typically achieve 70-90% degradation of azo and cationic dyes over 90-180 min, with pseudo-first-order rate constants (k_{app}) generally in the range of 0.010-0.025 min^{-1} under comparable catalyst loadings and light intensities (Długosz et al. 2021; Wu et al. 2019; Zhang et al. 2021; Shekofteh-Gohari et al. 2015). In the present system, Congo Red and Methylene Blue degradation efficiencies of ~87.9% and ~86.9%, respectively, within 120 min, together with k_{app} values of ~0.022-0.023 min^{-1} (CR) and ~0.030-0.031 min^{-1} (MB), place the catalyst at the upper end of the performance spectrum for ZnO/Fe-oxide-based photocatalysts (Ho and McKay 1999; Langmuir 1918).

Moreover, many reported Ag/ZnO or ZnO/Fe_3O_4 composites exhibit satisfactory photocatalytic activity but are challenging to recover, requiring centrifugation or filtration for reuse (Długosz et al. 2021; Wu et al. 2019). In contrast, the incorporation of Fe_3O_4 into the present ternary composite imparts magnetic separability, enabling rapid retrieval with an external magnet and minimal catalyst loss over five cycles, while still retaining ~88-89% degradation efficiency for both dyes. This combination of high activity plus magnetic recyclability is a notable advantage over non-magnetic counterparts (Długosz et al. 2021; Wu et al. 2019).

From a biological standpoint, reported Ag/ZnO and plant-mediated AgNP systems often show IC_{50} values in the range of 20-100 µg/mL against various cancer cell lines and moderate zones of inhibition (10-20 mm) against Gram-negative bacteria (Mosmann 1983; Bauer et al. 1966; Khan et al. 2019; Jayasri et al. 2025). The present nanocomposite demonstrates a highly potent IC_{50} of 17.77 ± 0.139 µg/mL against A549 cells and a 17 mm zone of inhibition against *Pseudomonas aeruginosa*, which is comparable to or better than many single-or binary-component systems synthesized via conventional chemical routes. Collectively, these comparisons confirm that the green-engineered Ag/ZnO/Fe_3O_4 nanocomposite performs on par with or exceeds several state-of-the-art nanocomposite photocatalysts reported in the literature.

5.2 Advantages of dual-extract green synthesis

The use of a 1:1 dual-extract blend of *Murraya koenigii* and *Cissus quadrangularis* introduces several distinct advantages over traditional single-extract or purely chemical synthesis routes. First, the combined phytochemical pool including carbazole alkaloids, flavonoids, phenolics, stilbenes, terpenoids and ascorbic acid derivatives provides a richer spectrum of reducing and capping agents, which promotes efficient nucleation, controlled growth and robust surface passivation of the Ag/ZnO/Fe_3O_4 nanocrystallites (Alam et al. 2014; Nazneen et al. 2020; Nocedo-Mena et al. 2024). This is reflected in the small primary particle sizes (6-18 nm), well-defined crystalline phases, and stable ternary architecture observed in TEM, XRD and Raman analysis (Długosz et al. 2021; Wu et al. 2019).

Second, the phytochemical corona originating from both plants yields an oxygen-

and heteroatom-rich surface with abundant –OH, –COOH, –OCH_3 and aromatic groups, which enhances dye adsorption, modulates surface charge, and facilitates intimate interfacial contact between the catalyst and pollutant molecules (Agarwal et al. 2017; Al-Darwesh et al. 2024). These features are consistent with the high Langmuir monolayer capacities and strong dye–catalyst affinities inferred from adsorption isotherm and kinetic analyses, ultimately translating into faster degradation rates and efficient ROS-driven mineralization (Langmuir 1918; Ho and McKay 1999).

Third, the dual-extract strategy eliminates the need for toxic reductants, surfactants or high-temperature organic solvents, offering a low-cost, environmentally benign, and scalable synthetic route well aligned with sustainable chemistry principles. The process conditions (60 °C extract activation, aqueous media, moderate calcination) are compatible with bulk or semi-pilot scale production, making the material attractive for practical wastewater treatment and antimicrobial surface applications.

5.3 Limitations and trade-offs of dual-extract synthesis

Despite its strengths, the dual-extract green synthesis approach also presents certain limitations and trade-offs compared to conventional chemical or single-extract methods. A primary challenge is the intrinsic compositional variability of plant extracts, which can depend on factors such as plant origin, harvest season, extraction conditions and storage, potentially leading to batch-to-batch fluctuations in nanoparticle size, surface chemistry, and activity (Agarwal et al. 2017; Al-Darwesh et al. 2024). This variability may complicate meeting strict reproducibility requirements for industrial-scale production and regulatory approval.

Additionally, the presence of abundant organic residues and carbonaceous species from the dual plant matrix can promote secondary aggregation in aqueous suspension, as evidenced by the large hydrodynamic sizes (~1420 nm) and high PDI (~0.85) observed in DLS measurements, despite the nanoscale primary particle sizes seen in TEM (Długosz et al. 2021). While such aggregates remain catalytically active and magnetically recoverable, they may reduce accessible surface area and hinder mass transfer in specific flow-through reactor configurations.

Another trade-off is that the composite's weak direct DPPH scavenging activity indicates that the phytochemical layer, after calcination and nanocomposite formation, primarily supports a pro-oxidant, ROS-dominated mechanism rather than classical antioxidant protection (Blois 1958; Kedare and Singh 2011; Gulçin 2023). This is advantageous for photocatalysis and cancer cell killing but may limit applications where strong radical-scavenging behaviour is desired. Finally, the complex multi-component nature of the dual-extract derived coating can make precise mechanistic deconvolution more challenging than in systems capped with well-defined synthetic ligands.

Overall, however, the performance gains, eco-friendly synthesis, magnetic recyclability and multifunctional biological photocatalytic properties afforded by the dual-extract Ag/ZnO/Fe_3O_4 nanocomposite clearly outweigh these limitations, positioning it as a promising, green alternative to many current state-of-the-art nanocomposite systems (Długosz et al. 2021; Wu et al. 2019; Zhang et al. 2021; Jayasri et al. 2025).

6. Environmental and Biomedical Implications

6.1 Recyclability and eco-toxicity considerations

The Ag/ZnO/Fe_3O_4 nanocomposite retained ~88-90% photocatalytic efficiency even after five cycles of reuse, confirming strong operational stability and recyclability (Długosz et al. 2021; Wu et al. 2019; Zhang et al. 2021; Ho and McKay 1999)**.** The magnetic Fe_3O_4 component enables rapid catalyst recovery using an external magnet, avoiding filtration or centrifugation steps and preventing nanoparticle leakage into aquatic systems (Długosz et al. 2021; Wu et al. 2019)**.** This magnetic separability minimizes

secondary sludge formation and reduces environmental release, making the material advantageous for sustainable water-treatment applications (Długosz et al. 2021; Wu et al. 2019; Zhang et al. 2021; Ho and McKay 1999)**.**

The weak antioxidant response in the DPPH assay, in contrast to strong photocatalytic ROS generation, indicates that the nanocomposite primarily behaves as a surface-reactive pro-oxidant rather than a freely diffusive radical generator in aquatic environments (Blois 1958; Kedare and Singh 2011; Gulçin 2023; Jayasri et al. 2025). In addition, the phytochemical capping derived from *Murraya koenigii* and *Cissus quadrangularis* contributes to biocompatibility, partial biodegradability, and suppression of excessive Ag^+ leaching (Agarwal et al. 2017; Alam et al. 2014; Nazneen et al. 2020; Nocedo-Mena et al. 2024). Together, these features demonstrate that the catalyst offers high activity with reduced eco-toxicity risk, supporting its safe implementation in water-remediation systems.

6.2 Antimicrobial and anticancer prospects

The nanocomposite exhibited a 17 mm zone of inhibition against *Pseudomonas aeruginosa*, confirming significant antibacterial activity against a multidrug-resistant Gram-negative pathogen (Bauer et al. 1966; Khan et al. 2019; Jayasri et al. 2025). The antimicrobial mechanism arises from a combination of Ag-mediated membrane disruption, ZnO-induced ROS generation, and Fe_3O_4-assisted electron transport, collectively triggering oxidative stress and bacterial cell damage (Długosz et al. 2021; Wu et al. 2019; Zhang et al. 2021). The phytochemical capping also enhances surface adhesion and contact-dependent bactericidal effects (Agarwal et al. 2017; Alam et al. 2014).

The strong anticancer response against A549 lung carcinoma cells ($IC_{50} \approx 17.77 \pm 0.139$ µg/mL) confirms a potent cytotoxic profile (Mosmann 1983; Jayasri et al. 2025). The mechanism is attributed to mitochondrial dysfunction, membrane destabilization, and ROS-driven apoptosis rather than classical antioxidant action (Blois 1958; Kedare and Singh 2011; Gulçin 2023). These findings suggest promising potential for applications in anticancer coatings, nano-therapeutic implants, photodynamic therapy platforms, and antimicrobial wound-care materials, subject to further in-vivo validation.

6.3 Industrial wastewater applicability

The efficient photo-degradation of both Congo Red (~87.9%) and Methylene Blue (~86.9%) under visible-light irradiation demonstrates broad applicability across different dye classes (Długosz et al. 2021; Wu et al. 2019; Zhang et al. 2021; Ho and McKay 1999). The high monolayer adsorption capacity derived from the Langmuir isotherm (q_{max} = 40 mg/g for CR and 45 mg/g for MB) indicates strong surface affinity and enhanced pollutant interaction (Langmuir 1918; Ho and McKay 1999). Coupled with fast charge-carrier transfer dynamics and high ROS generation efficiency, the composite enables rapid mineralization of dye contaminants commonly encountered in textile, printing, leather, and pharmaceutical wastewater streams**.** The ability to maintain high catalytic performance after multiple reuse cycles, together with magnetic recovery and phytochemical-driven surface stabilization, underscores the system's industrial practicality, reduced operational costs, and low environmental footprint (Agarwal et al. 2017; Długosz et al. 2021). Furthermore, the coexistence of photocatalytic decontamination and antibacterial activity renders the nanocomposite particularly valuable for industrial settings where chemical pollution and microbial contamination co-occur (Bauer et al. 1966; Khan et al. 2019; Jayasri et al. 2025).

CONCLUSION

In summary, a sustainable and eco-friendly strategy for the synthesis of a multifunctional $Ag/ZnO/Fe_3O_4$ nanocomposite was successfully developed using a dual-plant extract system derived from *Murraya koenigii* and *Cissus quadrangularis*. The phytochemical- assisted green synthesis

enabled efficient nucleation, surface functionalization, and stabilization of the ternary nanocomposite, resulting in a well-integrated plasmonic semiconducting magnetic architecture. Comprehensive physicochemical characterization confirmed the material's crystalline nature, nanoscale morphology, visible-light absorption capability, and soft-ferromagnetic behaviour.

The Ag/ZnO/Fe_3O_4 nanocomposite exhibited excellent photocatalytic performance toward both anionic and cationic dyes under visible-light irradiation, following pseudo-first-order kinetics and Langmuir adsorption behaviour. The enhanced activity is governed by a plasmon-assisted Z-scheme charge-transfer mechanism that promotes efficient charge separation and reactive oxygen species generation. Importantly, magnetic recoverability enabled facile catalyst recycling with sustained degradation efficiency over multiple cycles, highlighting its practical applicability.

Beyond environmental remediation, the nanocomposite demonstrated notable antibacterial activity against *Pseudomonas aeruginosa* and strong cytotoxic effects against A549 lung carcinoma cells, underscoring its multifunctional potential. Collectively, the combination of green synthesis, high photocatalytic efficiency, magnetic recyclability, and biological activity makes the Ag/ZnO/Fe_3O_4 nanocomposite a promising candidate for sustainable wastewater treatment, antimicrobial applications, and advanced environmental technologies.

Acknowledgements: This is not applicable.

Funding: This research received no external funding.

Authors' Contributions:

Vidusha Singh: Conceptualization, methodology, investigation, data analysis, writing original draft, and writing review and editing.

Indrasheel: Data analysis, and writing review and editing.

Narendra Pratap Singh: Conceptualization, writing review and editing.

(All authors read and approved the final manuscript.)

Ethical Approval: This study involved in-vitro experiments using the A549 human lung carcinoma cell line. All experimental procedures were conducted in accordance with institutional and standard ethical guidelines for laboratory research. No human participants or animals were directly involved in this study.

Consent to Participate: Not applicable.

Consent for publication: All authors have reviewed the manuscript and consent to its publication.

Competing Interests: The authors declare no competing interests.

Data Availability Statement: The data supporting the findings of this study are available from the corresponding author upon reasonable request.

Clinical trial number: not applicable.

REFERENCES

Agarwal, H., Kumar, S. V., & Rajeshkumar, S. (2017). A review on green synthesis of zinc oxide nanoparticles: An eco-friendly approach. *Resource-Efficient Technologies, 3*(4), 406–413. https://doi.org/10.1016/j.reffit.2017.03.002

Agarwal, H., Kumar, S. V., & Rajeshkumar, S. (2017). Green synthesis of ZnO nanoparticles: A review of methods and characterization. *Journal of Photochemistry and Photobiology B: Biology, 171*, 1–17. https://doi.org/10.1016/j.jphotobiol.2017.04.021

Agarwal, H., Nakara, A., & Shanmugam, V. (2017). A review of plant-mediated synthesis of zinc oxide nanoparticles for self-cleaning textiles. *Environmental Nanotechnology, Monitoring & Management, 7*, 63–73.

Alam, M. N., Roy, N., & Bhowmik, A. (2014). *Murraya koenigii* leaf extract: An efficient green source for the synthesis of metal nanoparticles. *ACS Sustainable Chemistry & Engineering*, *2*(7), 1707–1713. https://doi.org/10.1021/sc5001057

Al-Darwesh, M. Y., Ibrahim, S. S., & Mohammed, M. A. (2024). A review on plant-extract-mediated green synthesis of zinc oxide nanoparticles and their biomedical applications. *Results in Chemistry*, *7*, 101368. https://doi.org/10.1016/j.rechem.2024.101368

Alhujaily, M., Albukhaty, S., Yusuf, M., Mohammed, M. K. A., Sulaiman, G. M., Alyamani, A. A., Albaqami, J., & AlMalki, F. A. (2022). Recent advances in plant-mediated zinc oxide nanoparticles and their biomedical relevance. *Bioengineering*, *9*(10), 541. https://doi.org/10.3390/bioengineering9100541

Asadullah, A., Ahmad, M., Khan, Z. A., & Ullah, S. (2020). Green synthesis of ZnO/GO composites for the photocatalytic degradation of methylene blue. *Journal of Materials Science: Materials in Electronics*, *31*, 14443–14457. https://doi.org/10.1007/s10854-020-03847-2

Asadullah, A., Ahmad, M., & Khan, Z. A. (2025). Green synthesis of zinc oxide nanoparticles using *Murraya koenigii* leaf extract and their anti-infective efficacy against drug-resistant bacteria. *Preprint/Early article*.

Bauer, A. W., Kirby, W. M. M., Sherris, J. C., & Turck, M. (1966). Antibiotic susceptibility testing by a standardized single disk method. *American Journal of Clinical Pathology*, *45*(4), 493–496. https://doi.org/10.1093/ajcp/45.4.493

Bhardwaj, A., Singh, A. K., & Ritika. (2024). *Murraya koenigii* plant-extract-mediated green synthesis of metallic nanoparticles and their applications. *Plant Nano*, *5*, 100076. https://doi.org/10.1016/j.plana.2024.100076

Blois, M. S. (1958). Antioxidant determinations by the use of a stable free radical. *Nature*, *181*, 1199–1200. https://doi.org/10.1038/1811199a0

Devadoss, D., Prakash, P., & Ramesh, S. (2023). Green-mediated copper oxide nanoparticles using *Murraya koenigii* leaves as a corrosion inhibitor. *Materials Today: Proceedings*, *72*, 2316–2323. https://doi.org/10.1016/j.matpr.2022.12.125

Długosz, O., Szostak, K., Krupiński, M., & Banach, M. (2021). Synthesis of Fe_3O_4/ZnO nanoparticles and their photocatalytic and magnetic properties. *Environmental Science and Pollution Research*, *28*, 6150–6165. https://doi.org/10.1007/s11356-020-10857-9

Elamin, N. Y., Hassan, M. M., & Abdelrahman, A. E. (2022). *Murraya koenigii* mediated synthesis of cobalt-doped NiO nanoparticles as eco-friendly bactericides. *Journal of Alloys and Compounds*, *918*, 165667. https://doi.org/10.1016/j.jallcom.2022.165667

Goudjil, M. B., Zeggai, F., & Chabane, S. (2024). Photocatalytic degradation of methylene blue using biosynthesized α-Fe_2O_3 nanoparticles. *Journal of Photochemistry and Photobiology A: Chemistry*, *453*, 114377. https://doi.org/10.1016/j.jphotochem.2024.114377

Gulçin, İ. (2023). DPPH radical scavenging assay: A current overview. *Processes*, *11*(8), 2248. https://doi.org/10.3390/pr11082248

Ho, Y. S., & McKay, G. (1999). Pseudo-second-order model for sorption processes. *Process Biochemistry*, *34*(5), 451–465. https://doi.org/10.1016/S0032-9592(98)00112-5

Jayasri, A., Kumar, R., & Singh, P. (2025). Green synthesis of silver and zinc oxide nanoparticles with veterinary applications. *Frontiers in Veterinary Science, 12*, 1521143. https://doi.org/10.3389/fvets.2025.1521143

Kalpana, V. N., Patra, R. R., & Rajeswari, V. D. (2017). Green synthesis of zinc oxide nanoparticles using fresh stem of *Cissus quadrangularis* extract and in-vitro studies. *Asian Journal of Chemistry, 29*(6), 1323–1327. https://doi.org/10.14233/ajchem.2017.20457

Kanimozhi, S., Balaji, S., & Ramesh, R. (2022). Biogenic synthesis of silver nanoparticles using *Cissus quadrangularis* stem extract and antibacterial activity. *Journal of Saudi Chemical Society, 26*(8), 101471. https://doi.org/10.1016/j.jscs.2022.101471

Kedare, S. B., & Singh, R. P. (2011). Genesis and development of DPPH method of antioxidant assay. *Journal of Food Science and Technology, 48*(4), 412–422. https://doi.org/10.1007/s13197-011-0251-1

Khan, Z. A., Siddiqui, M. F., & Park, S. (2019). Current and emerging methods of antibiotic susceptibility testing. *Diagnostics, 9*(2), 49. https://doi.org/10.3390/diagnostics9020049

Langmuir, I. (1918). The adsorption of gases on plane surfaces of glass, mica and platinum. *Journal of the American Chemical Society, 40*(9), 1361–1403. https://doi.org/10.1021/ja02242a004

Mamba, F. B., Moyo, M., & Ndlovu, N. (2024). Synergistic effect of ZnO/Ag_2O@g-C_3N_4 nanocomposites for degradation of organic dyes under visible light. *Applied Sciences, 14*(3), 1120. https://doi.org/10.3390/app14031120

Mosmann, T. (1983). Rapid colorimetric assay for cellular growth and survival. *Journal of Immunological Methods, 65*(1–2), 55–63. https://doi.org/10.1016/0022-1759(83)90303-4

Mutukwa, D., Ndlovu, N., & Moyo, M. (2024). Plant-mediated ZnO nanoparticles for antibacterial and photocatalytic applications. *Nanomaterials, 14*(14), 1182. https://doi.org/10.3390/nano14141182

Nath, A., Singh, R., & Kumar, P. (2025). Waste-derived green ZnO-Fe_2O_3 photocatalyst and polymer composite film for wastewater treatment. *Environmental Technology, 46*(1), 1–16. https://doi.org/10.1080/09593330.2024.2321145

Nazneen, S., Begum, S., & Rahman, A. (2020). Green synthesis and characterization of *Cissus quadrangularis* stem-mediated zinc oxide nanoparticles. *Plant Archives, 20*, 828–835.

Nocedo-Mena, D., Hernández-Sánchez, H., & Cruz-García, A. (2024). Nanoparticles derived from the *Cissus* genus and their biomedical applications. *Journal of Drug Delivery Science and Technology, 84*, 104560. https://doi.org/10.1016/j.jddst.2024.104560

Shekofteh-Gohari, M., Gohari, S., & Farhadi, S. (2015). Ternary ZnO/Ag_3VO_4/Fe_3O_4 nanocomposites: Magnetically separable photocatalysts under visible light. *Materials Chemistry and Physics, 163*, 107–116. https://doi.org/10.1016/j.matchemphys.2015.07.004

Sponza, D. T., & Korkmaz, M. (2023). Removal of Congo red and mordant dyes via ZnO/Fe_2O_3 nanocomposites. *American Journal of Scientific Research and Chemistry, 3*(1), 1–12.

Takcı, D. K., Aydin, A., & Yilmaz, M. (2024). Plant-mediated green route to the synthesis of zinc oxide nanoparticles and antimicrobial activity. *Green*

Processing and Synthesis, *13*, e01064. https://doi.org/10.1515/gps-2024-01064

Wu, Z., Zhang, L., & Li, Y. (2019). A ternary magnetic recyclable ZnO/Fe_3O_4/g-C_3N_4 photocatalyst with enhanced visible-light activity. *Nanomaterials*, *9*(4), 584. https://doi.org/10.3390/nano9040584

Zhang, P., Liu, Y., & Wang, X. (2021). Facile fabrication of magnetic Ag/ZnO/Fe_3O_4 composite with enhanced photocatalytic activity under simulated sunlight. *Materials Today Chemistry*, *20*, 100451. https://doi.org/10.1016/j.mtchem.2021.100451